Mass-selective neutron spectroscopy of lithium hydride and deuteride: Experimental assessment of the harmonic and impulse approximations

Maciej Krzystyniak* and Selena E. Richards
School of Science and Technology, Nottingham Trent University, Clifton campus, Nottingham NG11 8NS, United Kingdom and ISIS Facility, Rutherford Appleton Laboratory, Chilton, Didcot, Oxfordshire OX11 0QX, United Kingdom

Andrew G. Seel and Felix Fernandez-Alonso†
ISIS Facility, Rutherford Appleton Laboratory, Chilton, Didcot, Oxfordshire OX11 0QX, United Kingdom
(Received 26 July 2013; revised manuscript received 22 October 2013; published 19 November 2013)

Neutron Compton scattering experiments on crystalline lithium hydride and deuteride are presented and compared with existing experimental data and first-principles predictions. With currently available instrumentation, these measurements demonstrate sufficient mass selectivity for studies of nuclear-momentum distributions of protons, deuterons, and lithium using forward and backscattering geometries. In both materials, spectral discrimination of lithium-recoil features is highest in backscattering geometry, although mass isolation is also possible in the forward-scattering direction. These results evince the possibility of performing simultaneous mass-selective neutron spectroscopic studies for nuclei with $m > 4$ amu. We also provide an in-depth analysis and assessment of departures from the harmonic and impulse approximations as described by the celebrated Sears expansion of the dynamic structure factor, as well as how these can manifest themselves in the experimental data. We close by outlining the potential of our experimental strategy for mass-selective spectroscopic studies of materials containing protons and other light nuclides.

DOI: 10.1103/PhysRevB.88.184304 PACS number(s): 78.70.Nx, 29.30.Hs, 63.20.dk

I. INTRODUCTION

In recent studies,[1,2] Krzystyniak and Fernandez-Alonso presented the theoretical formalism for the prediction of nuclear-momentum distributions (NMDs) in crystalline materials by recourse to first-principles electronic-structure calculations within the framework of density-functional theory (DFT). In this approach, second moments (σ) and Laplacians ($\langle\nabla^2 V\rangle \equiv \Delta$) of the NMD were obtained from phonon-dispersion relations and atom-projected vibrational densities of states (VDOSs). To illustrate the method, this work also provided quantitative predictions for the underlying NMDs in face-centered-cubic (fcc) lithium hydride (LiH) and deuteride (LiD). Comparison with existing (albeit sparse) neutron-scattering data[3–5] served to demonstrate an excellent agreement between theory and experiment within the harmonic Born-Oppenheimer approximation (HBOA), as well as an upper bound of ∼2–3% for the effects on nonadiabatic dynamics on σ and Δ for hydrogen (H) in this benchmark system. Motivated by the above, a similar experimental-computational strategy has been applied in a simultaneous neutron-diffraction (ND) and neutron Compton scattering (NCS) study on the uptake of molecular hydrogen (H_2) by the alkali-graphite intercalation compound KC_{24}.[6]

On the experimental front, direct access to single-particle NMDs has been made possible via ongoing developments in NCS.[7–10] In brief, NCS can be regarded as a mass-selective spectroscopic technique where each atomic mass in the material contributes to the overall time-of-flight (TOF) spectrum in the form of a Doppler-broadened recoil peak.[8]

The use of epithermal neutrons with energies up to hundreds of eV (orders of magnitude above phonon energies in condensed matter) is thought to guarantee sufficiently high momentum transfers such that the width of recoil peaks in the energy domain can be related to the kinetic-energy distribution in momentum space of the target nucleus prior to the scattering event, i.e., the so-called impulse approximation (IA).[8]

In this context, Karlsson[11] has recently argued that, within the finite time scales associated with the NCS process, there exists a time distribution of individual neutron encounters leading to a considerable elastic slowing-down of the recoiling particle for long scattering times. Karlsson also argues that such an effect appears to be most pronounced in diatomic systems where high-frequency vibrational motions are preferential along the molecular axes. This result has important consequences for the general applicability of the IA in NCS, including its expected dependence on the magnitude of neutron-momentum transfer. Commonly referred to as "final-state effects" (FSEs), these departures from the IA are caused by interactions between the recoiling nucleus and its environment.[7,12] To date, FSEs in both molecular and condensed-matter systems have been treated within a perturbative approach known as the Sears expansion.[13,14]

In addition to the recent work of Karlsson mentioned above, we also note that the Sears expansion has also been criticized by Rinat,[15] and a more rigorous formalism has been proposed by Gersch, Rodriguez, and Smith.[16] Karlsson points out that the presence of a high-energy tail in the NCS profile appears to agree quite well with available experimental data, naturally leading to the conclusion that the free-recoil approximation is far from being fulfilled in this particular system. For both H_2 and D_2, it was also noted that FSE corrections do not necessarily decrease with momentum transfer, as expected if one is to adhere to the more conventional approach by Sears.

In this work, we explore the extent to which NCS data may be distorted due to departures from the IA via measurements on crystalline LiH and its deuterated counterpart LiD, two isoelectronic and isostructural insulators characterized by distinctly different vibrational manifolds and associated

 ©2013 American Physical Society

NCS recoil energies. LiH exhibits one of the largest known isotope effects upon hydrogen/deuterium (H/D) substitution in terms of lattice parameters, elastic constants, and Debye temperatures.[17] In this spirit, solid LiH and LiD therefore offer a convenient platform for an experimental assessment of the general validity of the IA for H, D, and lithium (Li), as well as possible deviations from commonly accepted theoretical predictions, as recently postulated by Karlsson.

On a more practical side, use of a forward-scattering geometry to obtain NCS data also enables us to explore the simultaneous investigation of H, D, and Li over a wide range of momentum transfers. In this spirit, the present work constitutes a timely extension of the recent study of Seel and co-workers[18] on Li and fluorine (F) in ^{7}LiF using a backscattering geometry. These ongoing developments seek to ascertain the merits and strengths of mass-selective neutron spectroscopy (MANSE) techniques over a wider range of atomic masses. To that end, the paper is organized as follows. First, the theory of NCS under the IA and details of the NCS measurements are introduced. Next, we present a detailed analysis of the LiH/LiD NCS data for H, D, and Li using a series of physical models to describe the underlying NMDs. In light of recently developed formalisms for the calculation of FSEs, putative deviations from the HBOA and IA are then assessed in detail. These results are also compared with existing *ab initio* calculations, as well as with previous NCS and inelastic neutron scattering (INS) data. Finally, we discuss the general implications of our results for ongoing and future NCS work, including its use as a mass-selective spectroscopic technique for the study of more complex materials.

II. THE IMPULSE AND HARMONIC APPROXIMATIONS IN NEUTRON COMPTON SCATTERING

In NCS, the energy and momentum transfers imparted by the neutron to the target nucleus are so high that the scattering process can be treated within the IA.[7,8,12,13,19–23] In this limit (i.e., infinite momentum transfer $\vec{q}$), the dynamic structure factor $S_{\rm IA}(\vec{q},\omega)$ is directly related to the NMD $n(\vec{p})$:

$$S_{\rm IA}(\vec{q},\omega) = \int n(\vec{p})\delta(\omega - \omega_r - \vec{q}\cdot\vec{p}/M)d\vec{p}\,. \quad (1)$$

For a given nucleus of mass M, the δ function in Eq. (1) is centered at the recoil energy $\omega_r = \hbar^2q^2/2M$. Mathematically, the dynamic structure factor $S_{\rm IA}(\vec{q},\omega)$ can be expressed in terms of a function $J(y,\hat{q})$ that depends both on a scaling parameter y and the unit vector $\hat{q} = \vec{q}/q$ along the direction of momentum transfer $\vec{q}$:

$$\begin{aligned} S_{\rm IA}(\vec{q},\omega) &= (M/\hbar^2q)\int n(\vec{p})\delta(y - \hat{q}\cdot\vec{p})d\vec{p} \\ &= (M/\hbar^2q)J(y,\hat{q}). \end{aligned} \quad (2)$$

The scaling parameter y is the so-called West-scaling variable, whose value is equal to the projection of the nuclear momentum $\vec{p}$ onto $\hat{q}$:[13,24]

$$y = \vec{p}\cdot\hat{q} = \frac{M}{\hbar^2q}(\omega - \omega_r) = \frac{M}{\hbar^2q}\left(\omega - \frac{\hbar^2q^2}{2M}\right). \quad (3)$$

The function $J(y,\hat{q})$ in Eq. (2) is the so-called directional Compton profile. This observable is proportional to the probability that a nucleus has a momentum component along the direction of $\hat{q}$. In an isotropic system, the specific direction of $\hat{q}$ is of no relevance, and the NMD reduces to the Compton profile $J(y)$, which represents the probability that an atom has a momentum component y along an arbitrary direction in space. The IA is tantamount to assuming that the observed Compton profile $J(y)$ is the Radon transform of the NMD via West scaling.[8]

Hereafter, q will be given in units of Å^{-1}, energy transfer ω in meV, and atomic mass in amu. With this choice of units, Planck's constant is given by $\hbar = 2.044\,58$ (meV amu)$^{1/2}$ Å.

For finite values of q, FSEs are routinely calculated using the method of Sears.[13] To this end, standard data treatments express the NCS profile $J(y)$ as a series of the form[23]

$$\begin{aligned} J(y) &= J_{\rm IA}(y) + J_{\rm FSE} \\ &= J_{\rm IA}(y) - \frac{A_3}{q}\frac{d^3}{dy^3}J_{\rm IA}(y) + \cdots, \end{aligned} \quad (4)$$

where $J_{\rm IA}(y)$ is the IA result.

In the above expression, the magnitude of FSEs, A_3, is related to the mean Laplacian of the interatomic potential with respect to the position of the scattering atom, Δ, via $A_3 = \frac{M\Delta}{36\hbar^2}$, where Δ is expressed in meV Å^{-2} (cf. Refs. 11, 23, and 25).

In an NCS experiment performed on an isotropic sample within the IA limit, a given NCS profile $J_{\rm IA}(y)$ can be related to a spherically averaged three-dimensional NMD $n_{\rm IA}(p)$ by the following expression:[8]

$$n_{\rm IA}(p) = \frac{-1}{2\pi y}\frac{\partial J_{\rm IA}(y)}{\partial y}\bigg|_{y=p}, \quad (5)$$

where the radial NMD, $n_{\rm IA}(p)$, can be represented as[8]

$$n_{\rm IA}(p) = \frac{\exp\left(\frac{-p^2}{2\sigma^2}\right)}{(\sigma\sqrt{2\pi})^3}\sum_n c_n(-1)^n L_n^{1/2}\left(\frac{p^2}{2\sigma^2}\right), \quad (6)$$

where $L_n^{1/2}$ denotes a generalized Laguerre polynomial. Equation (6) can be used for the reconstruction of $n_{\rm IA}(p)$ from the measured $J(y)$ after subtraction of the FSE contribution $J_{\rm IA}(y) = J(y) - J_{\rm FSE}$. To this end, $J_{\rm IA}(y)$ is fitted to a Gram-Charlier expansion of the form[8]

$$J(y) = \frac{\exp\left(\frac{-y^2}{2\sigma^2}\right)}{(\sigma\sqrt{2\pi})}\sum_n \frac{c_n}{2^{2n}n!}H_{2n}\left(\frac{y}{\sigma\sqrt{2}}\right), \quad (7)$$

where H_{2n} denotes a Hermite polynomial.

In Eq. (7), the term with $n = 0$ is set to unity due to the normalization of the NMD. Moreover, with c_1 set to zero, the kinetic energy E_k of a nucleus with mass M is related to σ via $E_k = 3\hbar^2\sigma^2/2M$. This relationship is independent of the precise values of the remaining coefficients c_n. Therefore, in practice, the fitting of $J_{\rm IA}(y)$ to the Gram-Charlier expansion amounts to varying both the width of the momentum distribution σ and the coefficients c_n with $n \geqslant 2$. We also note that the coefficients c_n in Eq. (7) are identical to the expansion coefficients in Eq. (6) for the radial momentum distribution, which is tantamount to an inversion procedure between $J_{\rm IA}(y)$ and $n_{\rm IA}(p)$.[26]

As discussed in more depth in previous works,[2] NMDs in a periodic solid are most conveniently described on the basis

of the projected VDOS within the framework of the Gaussian approximation (GA).[27] The basic assumption within the GA is that the momentum distribution of the nth nucleus along $\widehat{q}$ assumes a purely Gaussian functional form. This assumption also provides the basis for an alternative description of NMDs to the Gram-Charlier expansion shown in Eq. (7) in terms of multivariate Gaussians to account for nuclear vibrations along different spatial directions.[28–30] In either case, the second moment of the NMD for a given nucleus n and along $\widehat{q}$, $\sigma_n^2(\widehat{q})$, can be written as

$$\sigma_{Mn}(\widehat{q})^2 = \frac{M_n}{N_q\hbar^2}\sum_{q\in 1\mathrm{BZ}}\sum_{\lambda=1}^{N_\lambda}[\vec{e}_{\,n}(\lambda,\vec{q})\cdot\widehat{q}]^2 \times\frac{\omega(\lambda,\vec{q})}{2}\coth\left(\frac{\omega(\lambda,\vec{q})}{2k_BT}\right), \quad (8)$$

where $\omega(\lambda,\vec{q})$ are phonon energies and $\vec{e}_{\,n}(\lambda,\vec{q})$ are polarization vectors for a given nucleus n. The summation in Eq. (8) runs over all $\vec{q}$ vectors within the first Brillouin zone, where N_q is the number of these wave vectors, as well as over all phonon branches λ of the unit cell. In the particular case of LiH, $N_\lambda = 12$. This number of phonon branches arises from the use of a nonprimitive fcc unit cell in our previous DFT calculations,[2] yet this choice bears no consequence on computational predictions for NCS observables. It is also important to note that this treatment tacitly assumes the validity of the HBOA discussed earlier.

From Eq. (8), the spherically averaged value of the second moment of the NMD for a nucleus n, $\sigma_{Mn}(\widehat{q})^2$, can be obtained from the total VDOS projected onto nucleus n, $G_n(\omega)$,

$$\sigma_n^2 = \frac{M_n}{\hbar^2}\int G_n(\omega)\frac{\omega}{2}\coth\left(\frac{\omega}{2k_BT}\right)d\omega. \quad (9)$$

The partial or projected VDOS, $G_n(\omega)$, corresponds to the contribution from a given atom to the total VDOS. $G_n(\omega)$ is defined by the following sum over all q points in the first Brillouin zone and over all phonon bands:[1,3]

$$G_n(\omega) = \frac{1}{3N_q}\sum_{q\in 1\mathrm{BZ}}\sum_{\lambda=1}^{N_\lambda=12}\vec{e}_{\,n}(\lambda,\vec{q})^2\delta(\omega-\omega(\lambda,\vec{q})), \quad (10)$$

where $\vec{e}_{\,n}(\lambda,\vec{q})$, $\omega(\lambda,\vec{q})$, and N_q have been defined earlier when introducing Eq. (8). $G_n(\omega)$ for a harmonic solid can also be used to estimate the magnitude of FSEs introduced in Eq. (4). The spherical average of the Laplacian Δ for nucleus n can be written as[14]

$$\Delta = \frac{3M}{\hbar^2}\int\omega^2 G_n(\omega)d\omega. \quad (11)$$

For an isotropic three-dimensional harmonic oscillator (3D-HO) this quantity is given by[23]

$$\Delta = \frac{12\hbar^2\sigma^4}{M}. \quad (12)$$

The connection between the magnitude of FSEs [coefficient A_3 in Eq. (4)] and the spherical average of the Laplacian Δ was originally introduced by Sears:[13]

$$A_3 = \frac{M\Delta}{36\hbar^2}, \quad (13)$$

which, after some algebra, leads to an explicit relationship between A_3 and σ for the case of a 3D-HO:[11]

$$A_3 = \frac{\sigma^4}{3}. \quad (14)$$

The Gram-Charlier expansion given by Eq. (7) may then be modified to account for FSEs by writing

$$\frac{A_3}{q}\frac{d^3}{dy^3}J_{\mathrm{IA}}\left(\frac{y}{\sigma\sqrt{2}}\right) = \frac{k}{q}H_3\left(\frac{y}{\sigma\sqrt{2}}\right), \quad (15)$$

where A_3 is expressed through the expansion term k multiplying the third-order Hermite polynomial $H_3(\frac{y}{\sigma\sqrt{2}})$. Introducing the auxiliary variable $x = \frac{y}{\sigma\sqrt{2}}$ in the Gram-Charlier expansion such that $\frac{d^3}{dy^3}J_{\mathrm{IA}}(\frac{y}{\sigma\sqrt{2}}) = (\frac{1}{\sigma\sqrt{2}})^3\frac{d^3}{dx^3}H_3(x)$, one can finally write[2]

$$k = A_3\left(\frac{1}{\sigma\sqrt{2}}\right)^3 = \sigma\frac{\sqrt{2}}{12} \quad (16)$$

for a 3D-HO and, more generally,

$$k = A_3\left(\frac{1}{\sigma\sqrt{2}}\right)^3 = \frac{M\Delta}{36\hbar^2}\left(\frac{1}{\sigma\sqrt{2}}\right)^3 \quad (17)$$

for a harmonically bound nucleus with an underlying VDOS other than the simple 3D-HO case introduced above. It is worth noting that σ in Eq. (16) is obtained from the use of a single (effective) oscillator frequency used in 3D-HO models, whereas σ in Eq. (17) requires knowledge of a nucleus-projected VDOS using phonon-dispersion relations.

To obtain the radial momentum distribution $n_{\mathrm{IA}}(p)$ by means of the Gram-Charlier expansion, the FSE contribution J_{FSE} must first be calculated and then subtracted from the measured NCS profile $J(y)$. Mathematically, A_3 and σ are correlated as they are both functions of the same atom-projected VDOS. However, a simple analytical relation between A_3 and σ that can be used as a constraint in the fitting of experimental NCS profiles is only known for the 3D-HO case. Thus, in practice, only Eq. (16) is of practical utility in the analysis of experimental data. The task of subtracting J_{FSE} from the measured NCS profile $J(y)$ can be accomplished either by assuming that both A_3 (and hence k) and σ can be calculated from the 3D-HO model and using Eq. (16) as a constraint in the fitting of experimental NCS profiles. Alternatively, it is also possible to assume a more general form of the VDOS and relax both k and σ during the fitting procedure. In the present work, both methods have been applied for further comparison with HBOA predictions. For clarity, the relation $k = \sigma\frac{\sqrt{2}}{12}$ will be used hereinafter to describe the constraint applied to the description of experimental data within the framework of the 3D-HO model.

III. MATERIALS AND METHODS

A. NCS experiments

All measurements were carried out on VESUVIO, an indirect-geometry NCS spectrometer located at the ISIS Facility, Rutherford Appleton Laboratory, United Kingdom.[23,31] Both LiH and LiD were purchased from Sigma Aldrich as friable powders. To contain these samples, a set of two 6 × 6 cm^2

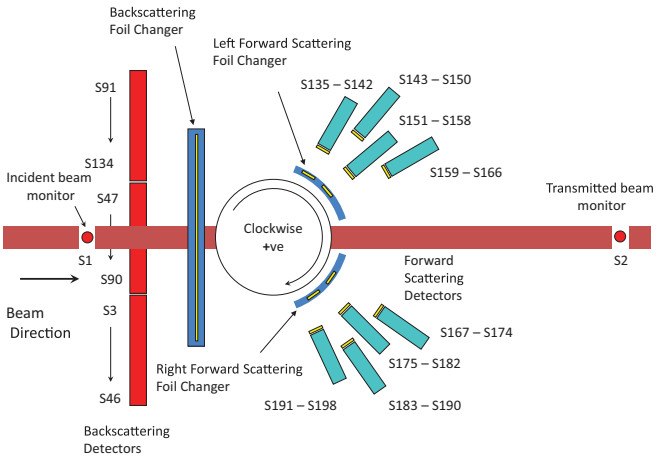

FIG. 1. (Color online) Schematic diagram of VESUVIO. For further details, see the text.

aluminum (Al) sachets were prepared from thin Al foil of thickness 50 μm. The LiH sample had a mass of 2.576 g. To compensate for a lower neutron-scattering cross section of the deuterated sample, a total of 13.590 g of LiD was used. Both LiH and LiD specimens were enclosed in the aforementioned Al sachets and further placed into two flat-can Al containers resulting in a total LiH (LiD) thickness of 4.3 (7.7) mm. The resulting scattering power of the LiH (LiD) sample was estimated to be 15% (10%). Both flat-geometry samples were carefully aligned perpendicular to the incident beam and NCS data collected at 300 K. Total integrated proton currents were 9200 and 5835 μA h for LiH and LiD, respectively.

On an indirect-geometry NCS spectrometer such as VESUVIO, the sample is exposed to a polychromatic neutron beam characterized by an incident-energy spectrum $I(E_0)$. Incident neutrons having initial energy E_0 travel a distance L_0 from the pulsed source to the sample. After scattering at an angle θ, neutrons of final energy E_1 travel a distance L_1 to the detector as schematically shown in Fig. 1. To achieve energy selection, a thin foil is placed in front of the detectors. This foil absorbs neutrons over a narrow range of energies, thereby fixing the final energy of the detected neutrons. For our NCS measurements on solid LiH and LiD, a gold (Au) foil was used to absorb neutrons at $E_1 = 4.9$ eV. With this experimental arrangement, data collection necessarily involves foil cycling in both forward and backscattering geometries in order to obtain TOF data with and without energy selection, followed by a subtraction of these two data sets to obtain NCS spectra. In this context, it is worth emphasizing that the "foil-out" data set in every VESUVIO experiment is tantamount to a simultaneous ND measurement of the sample under investigation, as recently demonstrated in *in situ* adsorption experiments.[6] We anticipate that future NCS work on increasingly complex materials will benefit greatly from the use of this (largely unexploited) capability of the instrument to perform concurrent structural and spectroscopic studies.

On VESUVIO, two different final-energy-selection schemes are currently used, hereafter referred to as resonance-detector (RD) and resonance-filter (RF) configurations.[9,32] The RD configuration employs the foil to define the energy of the scattered neutrons via resonant neutron absorption, and a γ-ray detector to probe the prompt cascade following the subsequent (n,γ) reaction. At present, VESUVIO uses RD (RF) in forward (backscattering) geometries, respectively.

For RD, the present forward-scattering bank uses yttrium-aluminum-perovskite-doped (YAP) γ-ray detectors,[9,33–35] designed to function both as neutron and energy selectors by placing a Au foil on the YAP-detector surface.[9,36] A secondary foil placed in two distinct positions is used to improve both energy resolution and signal-to-background ratios. In "foil-out" measurements, scattered neutrons only see the primary foil, whereas "foil-in" measurements require them to pass through the secondary foil prior to reaching the primary foil. The final NCS TOF spectrum in forward scattering is then obtained from subtraction of the "foil-in" from the "foil-out" raw data. This difference method removes most of the γ-ray background and also improves spectral resolution.

For the RF configuration, the VESUVIO backscattering bank is equipped with Li-doped glass detectors only sensitive to neutrons.[9] Using Au as energy-filter material, NCS TOF spectra in the backscattering direction are obtained by taking the difference between "foil-in" and "foil-out" data. This standard technique is referred to as single difference (SD). To improve final-energy resolution, double-difference (DD) techniques[37,38] have also been implemented with success. In this case, three measurements are necessary, namely with no filter, a filter of thickness d_1 and neutron absorption $A_1(E_1)$, and a filter of the same material of thickness d_2 and absorption $A_2(E_1)$. The DD technique relies upon the fact that when the neutron-absorption cross section $\sigma_A(E_1)$ is small, the following approximation becomes valid:

$$A_1(E_1) = 1 - \exp[-Nd_1\sigma_A(E_1)] \sim Nd_1\sigma_A(E_1) \qquad (18)$$

with an analogous expression for $A_2(E_1)$. The resulting DD signal S_{DD} can then be written as

$$S_{\mathrm{DD}}(E_1) = A_1(E_1) - \frac{d_1}{d_2}A_2(E_1). \qquad (19)$$

Because $\sigma_A(E_1)$ is negligibly small in the tail regions of the foil resonance, $S_{\mathrm{DD}}(E_1) = 0$ for significant offsets away from the resonance maximum. Thus, the long tails of the function $A_1(E_1)$ appearing in SD are strongly suppressed irrespective of their functional form, and energy resolution is therefore improved considerably. The energy resolution function is well approximated by a Voigt line shape,[23] where the Lorentzian contribution reflects the long tails. These are largely removed by the DD technique. Moreover, low-energy contributions to the resolution function arising from the $1/\sqrt{E_1}$ dependence[38–41] of the neutron-capture cross section of the analyzer foil are also suppressed in these DD measurements.

A schematic diagram of VESUVIO is shown in Fig. 1. The incident- and transmitted-beam monitors (S1 and S2) consist of beads of ^{6}Li-doped scintillator glass. In forward scattering, a total of 64 YAP detectors (S135–S198) are arranged into near-to-vertical columns of eight detectors, four above and below the horizontal plane passing through the sample center. Each detector element is 8 cm in height, 2.5 cm in width, and 0.6 cm in thickness.[42] The final neutron energy is fixed at 4897 meV, with an energy resolution function which is well described by the convolution of a Lorentzian of half-width

at half-maximum (HWHM) 24 meV and a Gaussian with standard deviation (STD) 73 meV.[43] In backscattering, there are a total of 132 ^{6}Li-doped glass scintillation detectors (S3–S134). DD techniques are used to define a final energy of 4897.3 meV. In this geometry, the resolution function is nearly Gaussian with extended (small) wings, and can be accurately described as the convolution of a Gaussian (STD = 74 meV) and a Lorentzian (HWHM = 24 meV).[42]

B. Data reduction and analysis

The total number of neutrons detected for a given mass M and TOF channel t on an indirect-geometry spectrometer is proportional to the NCS profile, $J[y_M(t)]$, convoluted in y_M space with a (mass-dependent) instrumental resolution function $R[y_M(t)]$. The resolution function $R[y_M(t)]$ can be expressed as a convolution of different contributions associated with uncertainties in L_0, L_1, θ, t, and E_1. The resolution calculation is performed by considering a mass- and TOF-dependent West-scaling variable $y_M(t)$ for each mass M as a function of other experimental variables, that is, $y_M = y_M(L_0,L_1,\theta,t,E_1)$. Uncertainties in these experimental variables are assumed to be independent of each other and sufficiently narrow for the differentials $\frac{\partial y_M}{\partial L_0}$, $\frac{\partial y_M}{\partial L_1}$, $\frac{\partial y_M}{\partial \theta}$, $\frac{\partial y_M}{\partial t}$, and $\frac{\partial y_M}{\partial E_1}$ to remain constant over their respective ranges.[32] Additionally, these uncertainties, denoted as ΔL_0, ΔL_1, $\Delta\theta$, Δt, and ΔE_{1g}, are assumed to obey normal Gaussian statistics. The resulting final resolution function $R[y_M(t)]$ then becomes a series of convolution products of the form

$$\begin{aligned} R[y_M(t)] &= R_{L0}[y_M(t)] \otimes R_{L_1}[y_M(t)] \otimes R_\theta[y_M(t)] \\ &\quad \otimes R_t[y_M(t)] \otimes R_{E_{1g}}[y_M(t)] \otimes R_{E_{1l}}[y_M(t)] \\ &= R_g[y_M(t)] \otimes R_{E_{1l}}[y_M(t)], \end{aligned} \tag{20}$$

which can be described as a Voigt profile with the STD of the Gaussian component, Δg, given by

$$\begin{aligned} \Delta g^2 &= \left|\frac{\partial y_M}{\partial L_0}\right|^2 \Delta L_0^2 + \left|\frac{\partial y_M}{\partial L_1}\right|^2 \Delta L_1^2 + \left|\frac{\partial y_M}{\partial \theta}\right|^2 \Delta\theta^2 \\ &\quad + \left|\frac{\partial y_M}{\partial t}\right|^2 \Delta t^2 + \left|\frac{\partial y_M}{\partial E_1}\right|^2 \Delta E_{1g}^2 \end{aligned} \tag{21}$$

and the HWHM of the Lorentzian component is given by $\Delta l = |\frac{\partial y_M}{\partial E_1}|\Delta E_{1l}$.

Table I lists STDs and HWHMs of the Gaussian and Lorentzian components of the resolution function $R[y_M(t)]$, respectively, for M = H, D, Li, and Al. These data correspond to TOF data for a total of four detectors chosen so as to span the entire forward scattering and backscattering angular range of VESUVIO. The Gaussian-distributed component of the energy resolution function $R_{E_{1g}}[y_M(t)]$ is the dominant term in $R_g[y_M(t)]$ for all masses other than the proton. For forward scattering, this contribution increases with M and decreases with θ, e.g., at $\theta = 33.1^\circ$, it is responsible for 69%, 91%, and 94% of Δg for M = D, Li, and Al, respectively, whereas at $\theta = 57.6^\circ$ it amounts to 52%, 87%, and 94%. In backscattering, the contribution from $R_{E_{1g}}[y_M(t)]$ still increases with M, yet it is almost constant as a function of scattering angle, amounting to 89%, 98%, and 99% of the total width of $R_g[y_M(t)]$. The situation is completely different for the resolution function of protons, where the dominant contribution comes from the angular component of the Gaussian-distributed resolution function $\Delta\theta$. This contribution increases with scattering angle and accounts for 90% and 98% of Δg at scattering angles of 33.1° and 57.6°, respectively. The ratio of the Lorentzian HWHM of $R[y_M(t)]$ to the HWHM of the Gaussian-distributed component in $R[y_M(t)]$ (calculated from the STD Δg) increases with M and decreases with θ for forward scattering, and is equal to 0.11, 0.16, 0.21, and 0.22 at $\theta = 33.1^\circ$ and 0.04, 0.12, 0.21, and 0.22 at $\theta = 57.6^\circ$ for M = H, D, Li, and Al, respectively. In backscattering, this ratio is practically independent of M and θ and it is equal to 0.17 for all masses under investigation. Thus, on the whole, the VESUVIO resolution function can be described adequately by a Voigt line shape with a dominating Gaussian component predominantly arising from either the angular resolution function (for protons) or from the resolution in final energy (for other masses).

TABLE I. Gaussian STDs and Lorentzian HWHMs of the resolution function $R[y_M(t)]$ for M = H, D, Li, and Al at four different scattering angles. The scattering angles θ = 33.1°, 57.6°, 160.8°, and 130.5° correspond to detectors S166, S143, S133, and S3, respectively. All resolution parameters have been calculated using error propagation and are expressed in Å^{-1}: $\Delta_{y_M} L_0 = |\frac{\partial y_M}{\partial L_0}|\Delta L_0$, $\Delta_{y_M} L_1 = |\frac{\partial y_M}{\partial L_1}|\Delta L_1$, $\Delta_{y_M}\theta = |\frac{\partial y_M}{\partial \theta}|\Delta\theta$, $\Delta_{y_M} t = |\frac{\partial y_M}{\partial t}|\Delta t$, and $\Delta_{y_M} E_{1g} = |\frac{\partial y_M}{\partial E_{1g}}|\Delta E_{1g}$. See the main text for further details.

θ	$\Delta_{y_M} L_0$	$\Delta_{y_M} L_1$	$\Delta_{y_M}\theta$	$\Delta_{y_M} t$	$\Delta_{y_M} E_{1g}$	Δg	Δl
M = H							
33.1	0.34	0.44	3.21	0.05	1.42	3.55	0.40
57.6	0.14	0.28	3.21	0.05	0.62	3.29	0.17
M = D							
33.1	0.76	0.91	3.17	0.05	3.19	4.65	0.89
57.6	0.45	0.63	3.08	0.1	1.91	3.71	0.53
130.5	0.10	0.54	0.67	0.3	1.82	2.04	0.40
160.8	0.11	0.65	0.33	0.2	1.85	2.00	0.38
M = Li							
33.1	2.66	2.99	3.11	0.1	11.1	12.20	3.1
57.6	1.6	1.87	2.9	0.2	6.69	7.70	1.87
130.5	0.31	0.84	0.54	0.3	5.07	5.19	1.04
160.8	0.29	0.83	0.26	0.2	4.72	4.81	0.97
M = Al							
33.1	10.3	11.4	3.09	0.1	43	45.77	12
57.6	6.12	6.82	2.84	0.2	25.5	27.25	7.13
130.5	1.11	2.52	0.50	0.3	17.9	18.12	3.69
160.8	1.03	2.37	0.23	0.2	16.4	16.60	3.38

For a total of N different masses present in the sample, the total count rate $C_\theta(t)$ at a fixed scattering angle θ is given by [cf. Eq. (2.24) in Ref. 23]

$$C_\theta(t) = A' \left[\frac{E_0 I(E_0)}{q}\right]_t \sum_{n=1}^{N} I_n M_n J_n[y_n(t)] \otimes R_n[y_n(t)], \tag{22}$$

where A' is a constant, and the mass-independent factor $[\frac{E_0 I(E_0)}{q}]_t$ is a function of the incident neutron spectrum,

$I[E_0(t)]$, the initial neutron energy, $E_0(t)$, and the momentum transfer $q(t)$, all functions of t (for further details, see Ref. 23). In Eq. (22), $J_M[y_M(t)]$ for a given mass M is given by Eq. (4). Integrated peak intensities I_M are proportional to the scattering power $I_M = AN_M\sigma_M$, where $\sigma_M = 4\pi b_M^2$ is the total (bound) neutron-scattering cross section.[23,44]

Using Eq. (22) as our starting point, the following data-reduction and analysis protocol was applied to the experimental data:

(i) Raw TOF spectra were obtained in both forward scattering and backscattering. Forward-scattering spectra were measured with 64 individual YAP detectors located at scattering angles ranging from 32° to 68° using an RD-SD configuration. Backscattering spectra were recorded by 102 individual Li-glass detectors located at scattering angles ranging from 130° to 163° using RF-DD.

(ii) In order not to introduce any bias into our data-reduction procedures, noisy detectors were excluded prior to any subsequent data analysis. This task was achieved via comparison of our data with lead (Pb) calibration runs measured before these experiments.

(iii) Multiple-scattering (MS) contributions were subtracted from the raw TOF spectra. In practice, the most troublesome MS component arises from double scattering off heavy atoms in the sample. Such a scattering process gives rise to a spurious peak in the TOF profile to the left of the single-scattering contribution from heavy atoms. MS involving protons, on the other hand, leads to a smooth background under the H peak. MS was calculated and subtracted from the raw (forward scattering and backscattering) spectra in a self-consistent manner using the MSSUB procedure.[45]

(iv) Following MS subtraction, forward-scattering TOF spectra were corrected to remove γ backgrounds. These backgrounds were calculated from raw forward-scattering spectra in a self-consistent manner using the BCORR procedure.[46] It is worth noting that, at present, backscattering spectra do not require any γ background corrections as this scattering geometry uses an RF-DD configuration.

(v) MS and γ-corrected TOF spectra in forward scattering exhibited three recoil features: a broad and relatively strong peak at shorter TOFs due to H/D, and two narrow peaks at longer TOFs corresponding to Li and Al. Due to the kinematic condition $\omega(t) = \frac{\hbar^2 q(\theta,t)^2}{2M}$ defining the center of the NCS profile for a given mass M, the strong H and D peaks appear at significantly different TOF values for different scattering angles θ. The H-peak position moves from ~320 μs at a scattering angle of 32° to ~160 μs at 68°. The D-peak position moves from ~350 μs at a scattering angle of 32° to ~280 μs at 68°. The positions of the Li and Al peaks remain practically constant over the whole range of forward-scattering angles. The Li peak is centered at ~350 μs, whereas the Al peak sits at ~370 μs. Partial TOF-peak separation between the H/D peaks and the Li and Al recoil peaks was achieved over the whole forward-scattering range, thus greatly facilitating subsequent H/D and Li line-shape analysis for LiH/LiD, respectively. In forward scattering, recoil peaks appeared on a flat featureless background with no offset.

(vi) The kinematic condition $\omega(t) = \frac{\hbar^2 q(\theta,t)^2}{2M}$ does not allow for single neutron-proton scattering events in backscattering. As a consequence, TOF spectra in backscattering exhibited two (three) recoil peaks for LiH (LiD). In this case, a broad and relatively strong peak at shorter TOFs arises from D, and two narrow peaks at longer TOFs come from Li and Al. Unlike in forward scattering, the strong D peak remained centered around 140 ± 10 μs at scattering angles in the range 130°–170°. Similar to forward scattering, the positions of the Li and Al peaks in LiH/LiD TOF spectra remained essentially constant over the whole range of backscattering angles. The Li peak was centered at ~280 μs, whereas the Al peak at ~350 μs. Thus, suitable discrimination between the D, Li, and Al recoil peaks was possible over the entire backscattering detector bank. However, and unlike forward scattering, recoil peaks appear on a nonuniform background, particularly around the center of the D-recoil peak. Such a complicated baseline could not be modeled with a low-degree polynomial, even in a piecewise manner. To circumvent these difficulties, treatment of the backscattering data required a different strategy. The Li and Al peaks were isolated by cropping the LiH/LiD TOF spectra over the range 200–400 μs and a line-shape analysis was performed for both Li and Al assuming that both peaks appear on a background described by a third-degree polynomial. Analysis of D-recoil peaks in backscattering was not attempted due to the dominance of the above-mentioned backgrounds between 50 and 200 μs. Work is underway to suppress these undesirable features from the NCS data.

(vii) Corrected TOF spectra containing multiple recoil peaks were fitted directly in TOF using Eq. (22) to describe the angle-dependent count rate $C_\theta(t)$ using a series of NCS profiles $J_M(y)$ to describe the NCS response of each nuclide of mass M. These $J_M(y)$ were expressed as a sum of the IA limit and FSE contributions, $J_{M_{\mathrm{IA}}}$ and $J_{M_{\mathrm{FSE}}}$, respectively. For the forward-scattering TOF data, $J_{M_{\mathrm{IA}}}$ for H (D) in LiH (D) are given by a Gram-Charlier expansion. For Li and Al, $J_{M_{\mathrm{IA}}}$ are taken as Gaussian NCS profiles. For backscattering TOF data, $J_{M_{\mathrm{IA}}}$ for Li was expressed as a Gram-Charlier expansion, whereas $J_{M_{\mathrm{IA}}}$ for Al was assumed Gaussian. As in previous NCS studies,[8] the Gram-Charlier expansion was truncated to second order via the inclusion of the coefficient c_4 [see Eq. (7) and the discussion below]. FSE corrections $J_{M_{\mathrm{FSE}}}$ were accounted for via the inclusion of terms proportional to H_3/q.[47] In the spirit of Eq. (22), all NCS profiles were convoluted with their respective mass-dependent resolution functions R_M.[8]

With the above protocol in mind, the following expression was used to describe the count rate at a given detector:

$$C(\theta = \mathrm{const}, t) = A' \frac{E_0 I[E_0]}{q} \left(J_L(x_L) \otimes R_L(x_L) + \sum_{M \neq M_L} J_M(x_M) \otimes R_M(x_M) \right) + B(t), \tag{23}$$

where

$$J_L(x_L) = \frac{\exp\left(-x_L^2\right)}{\sqrt{2\pi\sigma_L^2}} \left(1 + \frac{c_4}{32} H_4(x_L) - \frac{k}{q} H_3(x_L)\right) \tag{24}$$

and $L = (\mathrm{H,D})$ for forward scattering or $L = \mathrm{Li}$ for backscattering. Furthermore,

$$J_M(x_M) = \frac{\exp\left(-x_M^2\right)}{\sqrt{2\pi\sigma_M^2}}\left(1 - \frac{k}{q}H_3(x_M)\right) \qquad (25)$$

with $M = \mathrm{Li}$ in forward scattering and $M = \mathrm{Al}$ in both forward and backscattering. In these expressions, $x_i = (y_i - y_{0i})/(\sigma_i\sqrt{2})$, where y_{0i} is the shift of the position of the maximum from the center of the recoil line and σ_i is the STD of the momentum distribution for the ith mass. $B(t)$ is a TOF-dependent baseline modeled as a zeroth (third) degree polynomial for forward (backscattering) data. As illustrated below, all forward-scattering TOF data for LiH and LiD show a certain degree of partial overlap between Li and Al signals. To model the latter, a Gaussian NMD characterized by an STD $\sigma_{\mathrm{Al}} = 13.39$ Å^{-1} was assumed. This width was calculated from the Debye temperature of the material, $\Theta_{\mathrm{Al}} = 390$ K (Ref. 48), and was kept fixed during all fitting sessions. For all nuclei, the shifts y_{0M} of the NCS profiles were also fixed to zero throughout. Thus, there are at most three distinct parameters characterizing each NMD, namely its second moment σ, the expansion term k responsible for the magnitude of the FSEs, and the Gram-Charlier term c_4. This last parameter is related to the excess kurtosis δ of the single-particle NMD by $c_4 = \delta/3$, where $\delta = (\mu_4 - 3\langle\sigma^2\rangle^2)/\langle\sigma^2\rangle^2$, with μ_4 being the fourth moment of the momentum distribution.[49]

Average values of σ, c_4, and k were obtained by fitting individual TOF spectra over selected detector ranges. Before the calculation of averages across detector banks, outliers other than those arising from noisy and/or faulty detectors were rejected on the basis on the chi-square (χ^2) test of goodness-of-fit.[50] For the present analysis of raw TOF data, there are a total 1024 TOF data points between 50 and 561.5 μs, sampled every 0.5 μs. Rebinning of these data into groups of five TOF bins yields around 200 data points for subsequent data analysis. Given the small number of fitting parameters relative to the total number of TOF data points, the effective number of degrees of freedom ν thus remains at $\sim$200. The critical reduced χ^2 value with a statistical level of significance $\alpha = 0.05$ and $\nu \sim 200$ is around 1.2. Thus, the null hypothesis that data fits with reduced χ^2 values greater than 1.2 describe the TOF data well can be rejected with a statistical confidence of 95% (two STDs). Similar criteria to identify outliers from NCS data have been used and justified in previous studies[45] and form the basis of the PARMEAN routine used in the present data analysis.[51]

To check for possible departures from HBOA predictions, six different fitting sessions were performed for forward and backscattering data. The fitting models are summarized in Tables II and III. In all cases considered, the momentum distribution of the lightest nucleus L, that is, $L = \mathrm{H}$ (D) for LiH (LiD) forward-scattering data and $L = \mathrm{Li}$ for LiH (LiD) backscattering data, respectively, was modeled by a Gram-Charlier expansion. The momentum distributions of all remaining nuclei M, where $M = (\mathrm{Li,Al})$ in forward scattering and $M = \mathrm{Al}$ in backscattering, were modeled as Gaussians for both LiH and LiD.

The expansion terms k_M accounting for FSEs in heavier nuclei were constrained during fitting via the 3D-HO relation

TABLE II. Fitting models and associated parameters used to describe NMDs in forward scattering. F is used to denote a free fit parameter, whereas all other entries are either fixed or tied to already defined quantities.

Model	$\sigma_{\mathrm{H,D}}$	$k_{\mathrm{H,D}}$	$c_{4_{\mathrm{H,D}}}$	σ_{Li}	k_{Li}	$c_{4_{\mathrm{Li}}}$	σ_{Al}	k_{Al}	$c_{4_{\mathrm{Al}}}$
1	F	0	0	F	$\sigma_{\mathrm{Li}}\frac{\sqrt{2}}{12}$	0	13.39	$\sigma_{\mathrm{Al}}\frac{\sqrt{2}}{12}$	0
2	F	F	0	F	$\sigma_{\mathrm{Li}}\frac{\sqrt{2}}{12}$	0	13.39	$\sigma_{\mathrm{Al}}\frac{\sqrt{2}}{12}$	0
3	F	$\sigma_{\mathrm{H,D}}\frac{\sqrt{2}}{12}$	F	F	$\sigma_{\mathrm{Li}}\frac{\sqrt{2}}{12}$	0	13.39	$\sigma_{\mathrm{Al}}\frac{\sqrt{2}}{12}$	0
4	F	F	F	F	$\sigma_{\mathrm{Li}}\frac{\sqrt{2}}{12}$	0	13.39	$\sigma_{\mathrm{Al}}\frac{\sqrt{2}}{12}$	0
5	F	0	F	F	$\sigma_{\mathrm{Li}}\frac{\sqrt{2}}{12}$	0	13.39	$\sigma_{\mathrm{Al}}\frac{\sqrt{2}}{12}$	0
6	F	$\sigma_{\mathrm{H,D}}\frac{\sqrt{2}}{12}$	0	F	$\sigma_{\mathrm{Li}}\frac{\sqrt{2}}{12}$	0	13.39	$\sigma_{\mathrm{Al}}\frac{\sqrt{2}}{12}$	0

$k_M = \frac{\sqrt{2}}{12}\sigma_M$. As discussed in Sec. II, the choice of the simple 3D-HO model to account for the magnitudes of FSEs does not allow for a validation of more general phonon-dispersion relations and VDOSs obtained from, e.g., *ab initio* calculations. Such a choice of FSE model is justified by present limitations in the experimental technique to probe the details of the underlying NMD for heavier nuclei beyond their second moment.

Notwithstanding the above, our NCS data for lighter nuclei allow for a more quantitative assessment of more general relations between k_L and σ_L beyond the 3D-HO. To this end, we have set both σ_L and k_L as free-fit (unconstrained) parameters and compared the results of these fits with the corresponding *ab initio* predictions. In addition to the case of an undetermined relation between σ_L and k_L described above, two additional possibilities were tested, namely values for k_L were either constrained in fitting by the relation $k_L = \frac{\sqrt{2}}{12}\sigma_L$ [cf. Eq. (16)], or fixed to zero. Due to a significantly lower spectral resolution associated with the NCS response of the heavier masses, the Gram-Charlier coefficients c_4 for these nuclei were set to zero, that is, the underlying NMDs were assumed to be Gaussian. For the light nuclei, c_{4_L} were either free fit parameters or set to zero. In all cases, the width of the NMD for Al was fixed to the Debye value $\sigma_{\mathrm{Al}} = 13.39$ Å^{-1} and the NMD was assumed to be Gaussian.

Backgrounds were accounted for by adding a polynomial baseline $B(t)$ as described above [cf. Eq. (23)]. Due to the presence of a smooth and flat background in the

TABLE III. Fitting models and associated parameters to describe NMDs in backscattering. F is used to denote a free fit parameters, whereas all other entries are either fixed or tied to already defined free quantities.

Model	σ_{Li}	k_{Li}	$c_{4_{\mathrm{Li}}}$	σ_{Al}	k_{Al}	$c_{4_{\mathrm{Al}}}$
1	F	0	0	13.39	$\sigma_{\mathrm{Al}}\frac{\sqrt{2}}{12}$	0
2	F	F	0	13.39	$\sigma_{\mathrm{Al}}\frac{\sqrt{2}}{12}$	0
3	F	$\sigma_{\mathrm{Li}}\frac{\sqrt{2}}{12}$	F	13.39	$\sigma_{\mathrm{Al}}\frac{\sqrt{2}}{12}$	0
4	F	F	F	13.39	$\sigma_{\mathrm{Al}}\frac{\sqrt{2}}{12}$	0
5	F	0	F	13.39	$\sigma_{\mathrm{Al}}\frac{\sqrt{2}}{12}$	0
6	F	$\sigma_{\mathrm{Li}}\frac{\sqrt{2}}{12}$	0	13.39	$\sigma_{\mathrm{Al}}\frac{\sqrt{2}}{12}$	0

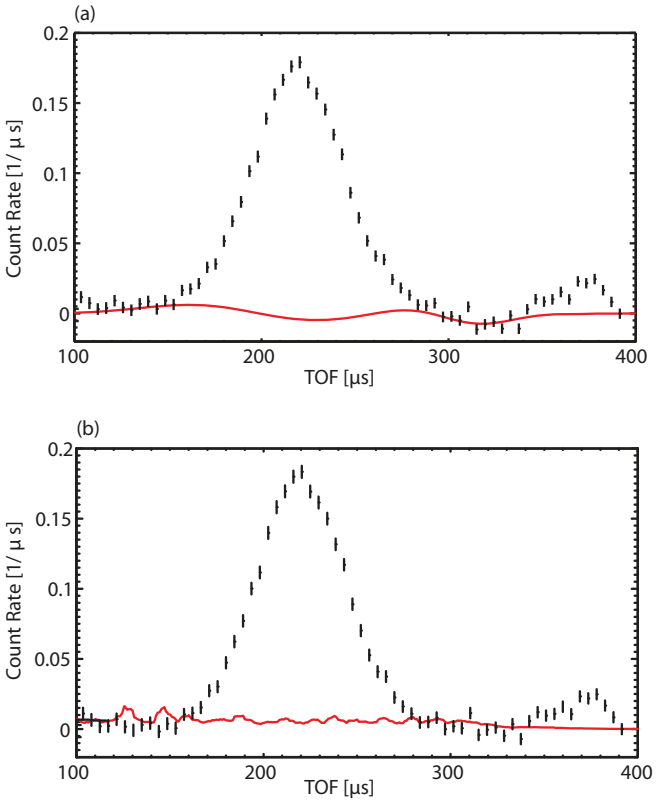

FIG. 2. (Color online) Representative LiH forward-scattering TOF spectrum at an angle of 58° (detector S143). (a) Raw data with γ-background correction shown in red; (b) data after γ-background corrections, with calculated MS corrections shown in red.

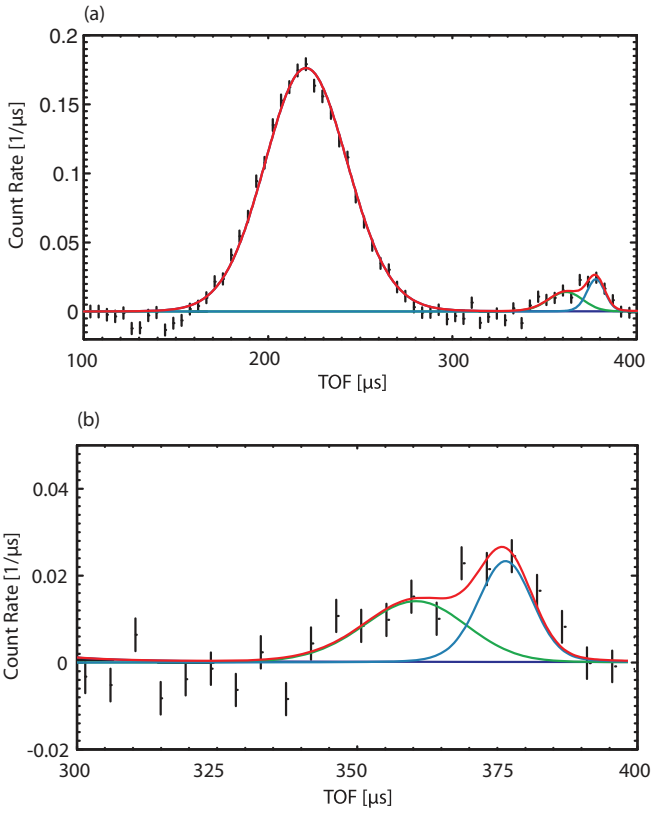

FIG. 3. (Color online) Representative LiH forward-scattering TOF spectra recorded at an angle of 58° (S143). Panel (a) shows the entire spectrum containing H, Li, and Al recoil peaks. Panel (b) shows the region of the TOF spectrum containing Li and Al. Individual contributions to the TOF spectrum from different masses are shown by thick colored lines, namely red (H and total), green (Li), and blue (Al). For further details, see the text.

forward-scattering TOF data, $B(t)$ was fixed to zero. In backscattering, the presence of a more complex background led to the choice of a third-order polynomial to describe $B(t)$. This choice was made by progressively increasing the polynomial degree of $B(t)$ until no further improvement in χ^2 values was observed.

IV. RESULTS

LiH forward-scattering spectra at an angle of 58° (detector S143) are shown in Figs. 2 and 3. Figure 2 shows the TOF data with γ background and MS corrections shown in red [panels (a) and (b), respectively]. Figure 3 shows these data after subtraction of the γ background and MS. The total fit shown corresponds to model 4 (cf. Table II) using Eq. (23) with NCS profiles described by Eqs. (24) and (25) for H and (Li,Al), respectively. The entire spectrum containing the H, Li, and Al recoil peaks is shown in panel (a). Panel (b) shows an expanded view of the TOF spectrum around Li and Al. The spectral response for LiH is clearly dominated by the strong scattering from H in this material. Notwithstanding this feature, it is still possible to discern contributions from heavier species in these single-detector data.

Analogous LiD TOF spectra are shown in Figs. 4 and 5. In both LiH and LiD, we observe a good degree of peak separation in forward scattering. The H/D peaks centered at small TOFs are essentially separated from the heavier-mass contributions arising from the presence of Li and Al. Moreover, a good degree of separation is also achieved between the recoil peak of Li and the Al sample can. In and of itself, this result demonstrates the ability of the NCS technique to perform MANSE studies in forward scattering for nuclei with masses greater than 4 amu.

Examples of LiH and LiD backscattering TOF spectra at an angle of 161° (detector S133) are shown in Figs. 6 and 7, respectively. Panel (a) of Figs. 6 and 7 shows raw data with MS contributions shown in red. Panel (b) in the same figures shows the raw data after subtraction of MS contributions and corresponding fits (model 4) using Eq. (23), with Compton profiles described by Eqs. (24) and (25) for Li and Al, respectively. Individual contributions from different masses are shown by thick colored lines: green for Li, blue for Al, and red for the total signal. In both cases, these data show an excellent degree of mass separation for Li and Al in backscattering geometry. This result further corroborates the ability of the TOF technique to separate nuclei with $m > 4$ amu, as also shown by Seel *et al.*[18] in recent MANSE studies of Li and F in ^{7}LiF using the same setup in backscattering.

In the fitting sessions associated with model 4 (cf. Tables II and III), σ, k, and c_4 for H and D were all free parameters in forward scattering. The momentum distributions of Li and Al were assumed to be Gaussian with the expansion terms k responsible for the magnitude of the FSEs constrained

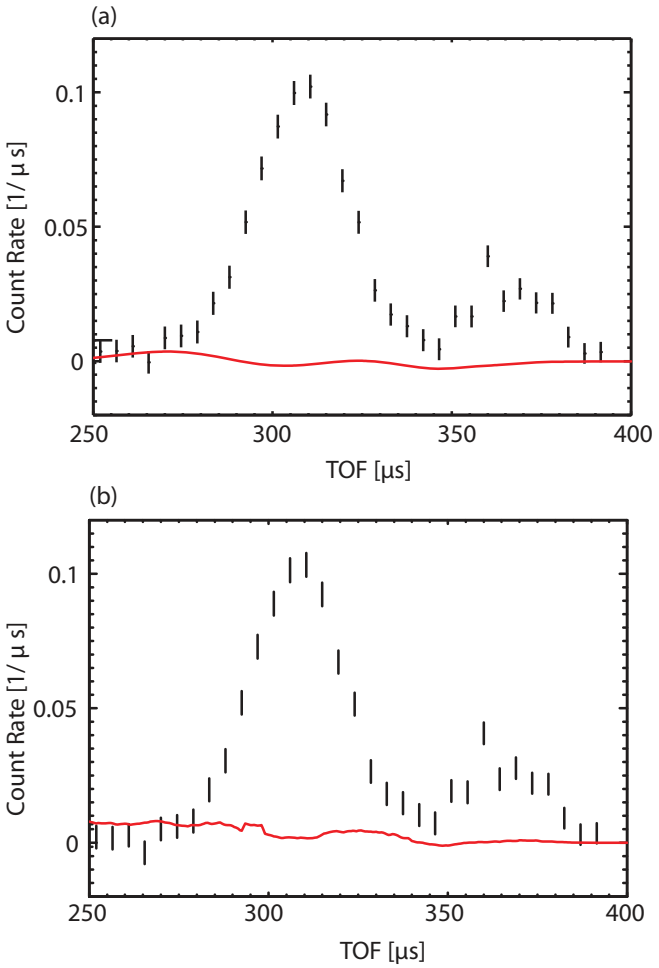

FIG. 4. (Color online) Representative LiD forward-scattering TOF spectrum at an angle of 58° (detector S143). (a) Raw data with γ-background correction shown in red; (b) data after γ-background corrections, with calculated MS corrections shown in red.

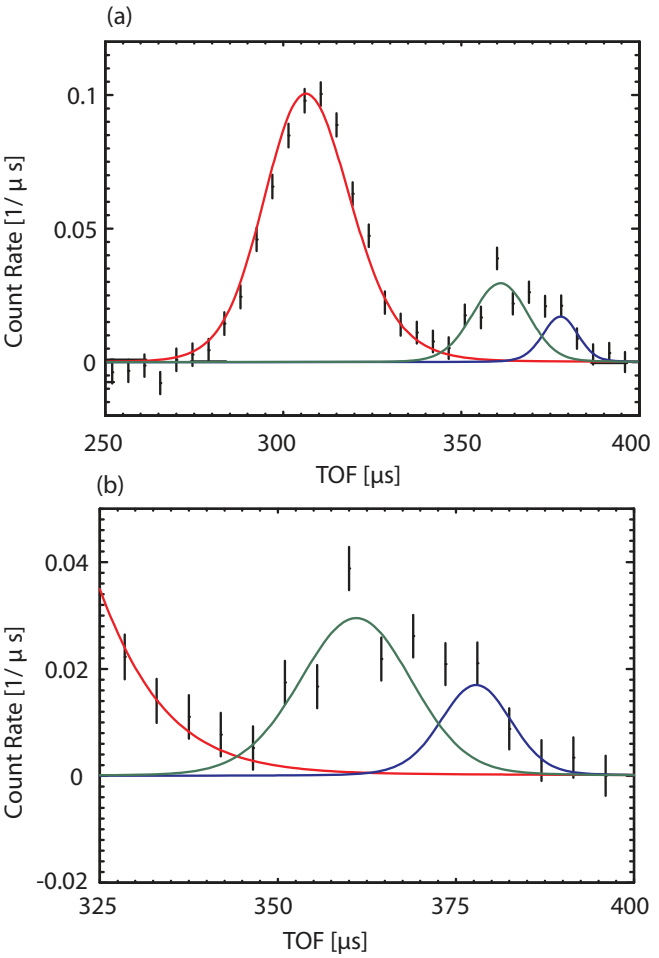

FIG. 5. (Color online) Representative LiD forward-scattering TOF spectra recorded at an angle of 58° (S143). Panel (a) shows the entire spectrum containing D, Li, and Al recoil peaks. Panel (b) shows the region of the TOF spectrum containing Li and Al. Individual contributions to the TOF spectrum from different masses are shown by thick colored lines, namely red (D and total), green (Li), and blue (Al). For further details, see the text.

using the result obtained from the simple 3D-HO model, $k_{\mathrm{Li,Al}} = \frac{\sqrt{2}}{12}\sigma_{\mathrm{Li,Al}}$. For the backscattering data, σ_{Li}, k_{Li}, and $c_{4_{\mathrm{Li}}}$ were also free fit parameters and the momentum distribution of Al was assumed to be Gaussian with the expansion term k constrained using the relation $k_{\mathrm{Al}} = \frac{\sqrt{2}}{12}\sigma_{\mathrm{Al}}$. In all cases, Al widths were fixed to the Debye value $\sigma_{\mathrm{Al}} = 13.39$ Å^{-1} as detailed in Sec. III. Results for LiH forward scattering and backscattering data are shown in Figs. 8 and 9. Analogous results for LiD are presented in Figs. 10 and 11.

Our results using model 4 in both forward and backscattering geometries not only provide a satisfactory description of the experimental data, but they also yield values for σ and c_4 for H, D, and Li with no apparent angular dependence within a statistical confidence band of two STDs (2-STD). Moreover, c_4 coefficients stay close to zero within this 2-STD confidence band. As model 4 imposes no constraints between fit parameters, it may be regarded as the most general NMD of the set. In terms of an underlying physical model, model 4 makes therefore no assumptions about harmonicity or the underlying phonon-dispersion relations or VDOS for these three light nuclides. Moreover, as fits are performed sequentially one detector at a time, this model does not constrain the fitted parameters obtained at different scattering angles (and corresponding to different amounts of energy and momentum transfers). Hence, model 4 allows in principle to ascertain the presence of nonadiabatic effects, as these would manifest themselves in terms of energy- and momentum-transfer-dependent NMDs, i.e., the appearance of additional, energy-shifted NMDs associated with the participation of excited electronic states in the scattering process. In light of the above remarks, the observed constancy in σ and c_4 values for H, D, and Li constitutes strong evidence for the absence of statistically significant effects associated with nonadiabatic dynamics over the whole range of forward and backscattering angles in both LiH and LiD, regardless of the degree of harmonicity or the specific details of the underlying phonon-dispersion relations dictating the vibrational dynamics of H, D, and Li in these two materials.

Due to its generality, model 4 can also be used to examine possible departures from the Sears model of FSEs in the context of the recent theoretical work Karlsson.[11] Figures 8 and 9 (10 and 11) report results for H, D, and Li using model

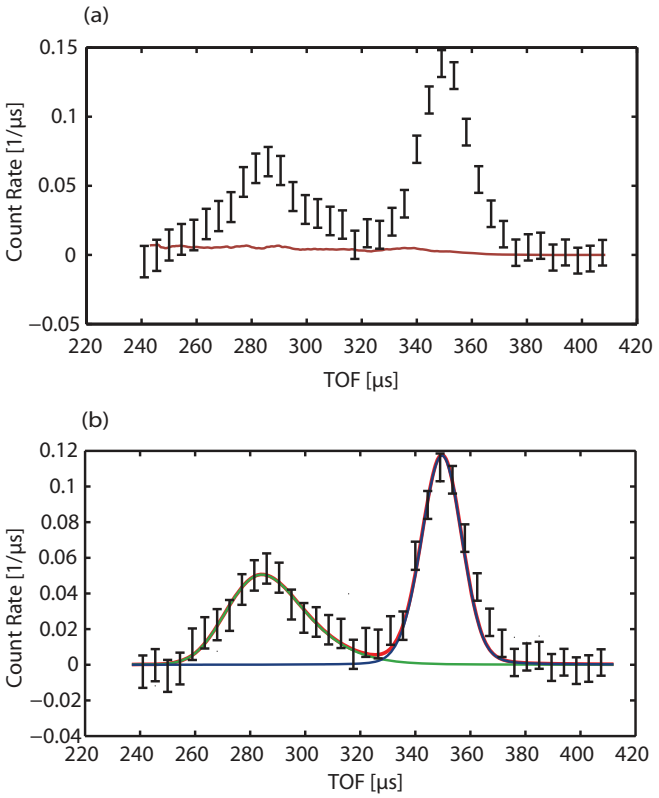

FIG. 6. (Color online) Representative LiH backscattering TOF spectrum at an angle of 161° (detector S133). (a) Raw data with MS contributions shown in red; (b) data after the subtraction of MS. See text for further details.

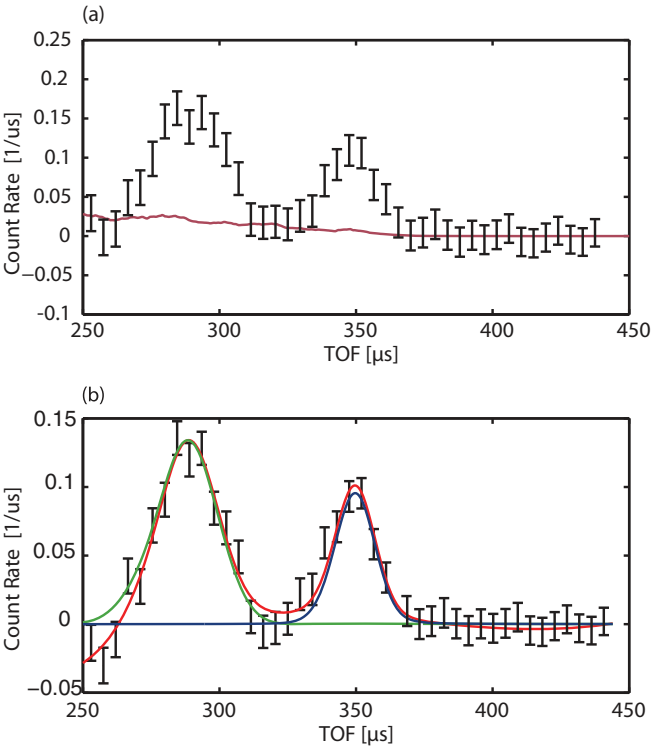

FIG. 7. (Color online) Representative LiD backscattering TOF spectrum at an angle of 161° (detector S133). (a) Raw data with the multiple scattering contribution shown in red; (b) data after the subtraction of the multiple scattering contribution. See text for further details.

4. Inspection of theses figures shows that although no trends are visible for LiD in both forward and backscattering, a linearlike trend for k_{H} in LiH as a function of angle cannot be entirely excluded. In this case, the values of k remain constant and within 3D-HO values below 45°, yet they appear to grow in absolute magnitude with increasing scattering angle. The absence of a similar behavior for D and Li in both forward and backscattering would be in line with the established view that FSEs are satisfactorily accounted for by the Sears expansion for nuclei other than H.[8] Moreover, whereas the fitted values of k for D and Li stay within the value $k = \frac{\sqrt{2}}{12}\sigma$, this behavior does not seem to apply for H in LiH. As discussed in Sec. II, the link between k and the NMD width σ is entirely dependent on the underlying vibrational dynamics, and a simple analytical relation between these two parameters is only known for an Einstein solid, yet we stress that model 4 makes no underlying assumption about correlations between these two physical parameters. The quality of the present experimental data does not allow us to be conclusive within comfortable levels of statistical confidence (i.e., $\geqslant$ 2-STD) and, therefore, we must defer a more detailed assessment of these (quite weak) trends to future investigations.

The above results are further corroborated by the sums of unit-area-normalized LiH and LiD TOF spectra measured by individual detectors in forward and backscattering, as well as by a comparison of this figure of merit with the sum of fitted curves representing unit-area-normalized expressions for $C(\theta = \mathrm{const}, t)$, i.e., $\sum_{i=1}^{N} \frac{C(\theta_i = \mathrm{const}, t)}{\int C(\theta_i = \mathrm{const}, t)dt}$ (cf. Figs. 12 and 13).

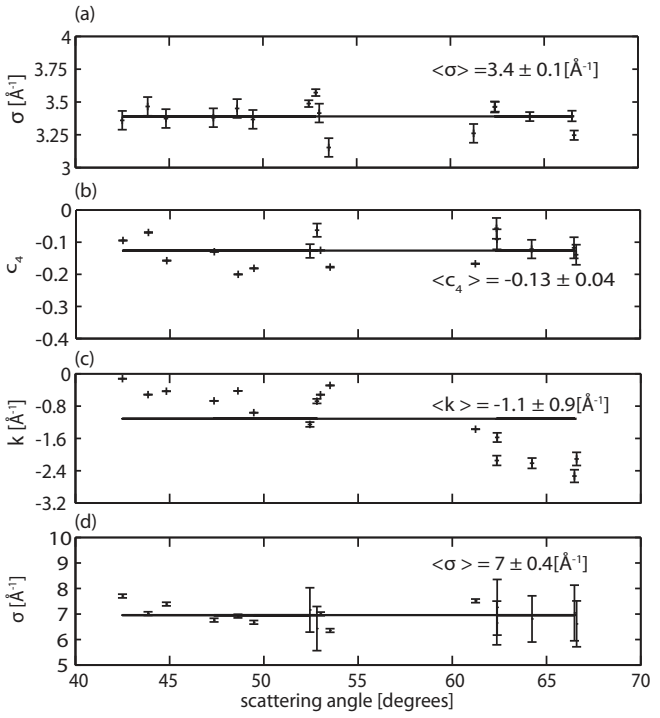

FIG. 8. Results for LiH forward-scattering data using model 4 (cf. Table II): (a) σ_{H}, (b) $c_{4_{\mathrm{H}}}$, (c) the expansion term k_{H} responsible for the magnitude of FSEs, and (d) σ_{Li}. Solid lines represent average values. For more details, see the text.

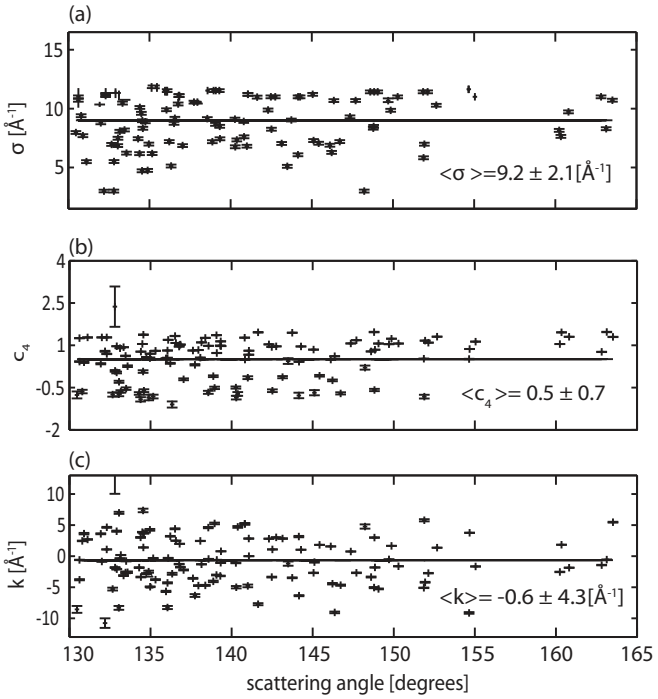

FIG. 9. Results for LiH backscattering data using model 4 (cf. Table III): (a) σ_{Li}, (b) $c_{4_{\mathrm{Li}}}$, and (c) the expansion term k_{Li} responsible for the magnitude of FSEs. Solid lines represent average values. For more details, see the text.

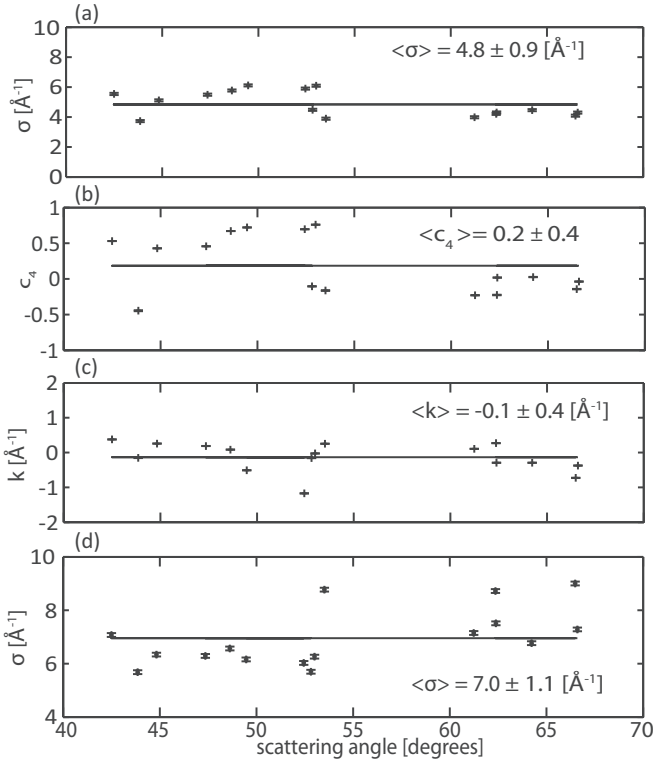

FIG. 10. Results for LiD forward-scattering data assuming model no. 4 (cf. Table II): (a) σ_{D}, (b) $c_{4_{\mathrm{D}}}$, (c) the expansion term responsible for the magnitude of the FSEs k_{D}, and (d) σ_{Li}. Solid lines represent average values. For more details, see the text.

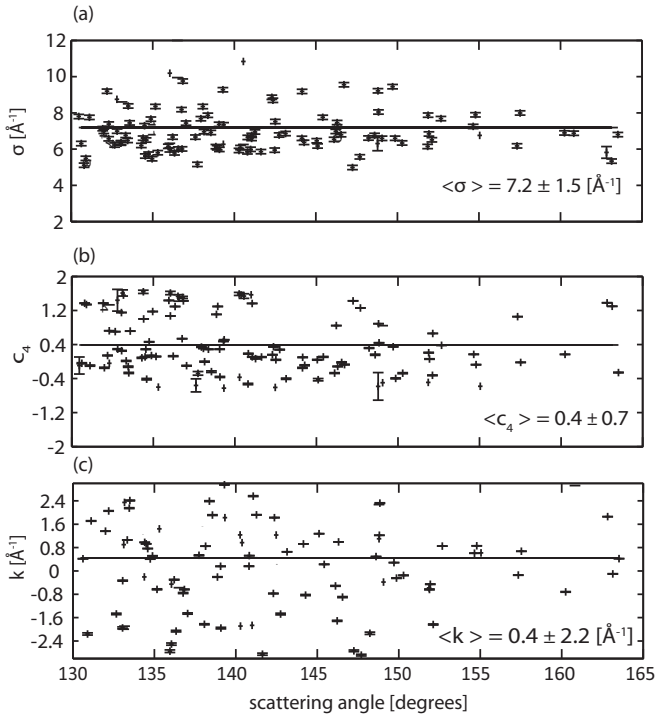

FIG. 11. Results for LiD backscattering data assuming model 4 (cf. Table III): (a) σ_{Li}, (b) $c_{4_{\mathrm{Li}}}$, and (c) the expansion term k_{Li} responsible for the magnitude of FSEs. Solid lines represent average values. For more details, see the text.

The summation range for this quantity corresponds to a selection of detectors after exclusion of outliers and faulty detectors as described in Sec. III.

As shown in Figs. 12 and 13, the agreement between experimental data and associated fits of unit-normalized sums for LiH and LiD TOF spectra is very good both in forward and backscattering and within a 1-STD confidence band on individual count rates. These summed TOF data contain broad distributions from H (D) in LiH (LiD). This feature arises from purely kinematic considerations defining the center of NCS profiles, with H and D peaks appearing over a broad range of TOFs at different scattering angles θ. In backscattering [cf. Figs. 12(b) and 13(b)], such a dependence of recoil-peak TOF positions as a function of θ is far less pronounced. This situation offers the possibility of clean isolation of summed NCS data representing individual recoil peaks for $m > 1$ amu, as previously explored by the MANSE studies of Seel *et al.* in backscattering.[18] In addition, our results show that a similar strategy is also possible in forward scattering, as the sums of unit-normalized TOF data are resolved well enough to be unique functions of the underlying individual NMDs. This feature is further demonstrated in Figs. 12(a) and 13(a) showing the presence of distinct shoulders and subsidiary maxima in the H and D recoil spectra, as well as a reasonable degree of separation of Li and Al. It is also important to note that the insights brought forward by the analysis of these summed data are of direct relevance to the possibility of significant enhancements in effective count rates in NCS studies. With the present experimental setup on VESUVIO, these gains can be greater than two orders of magnitude,

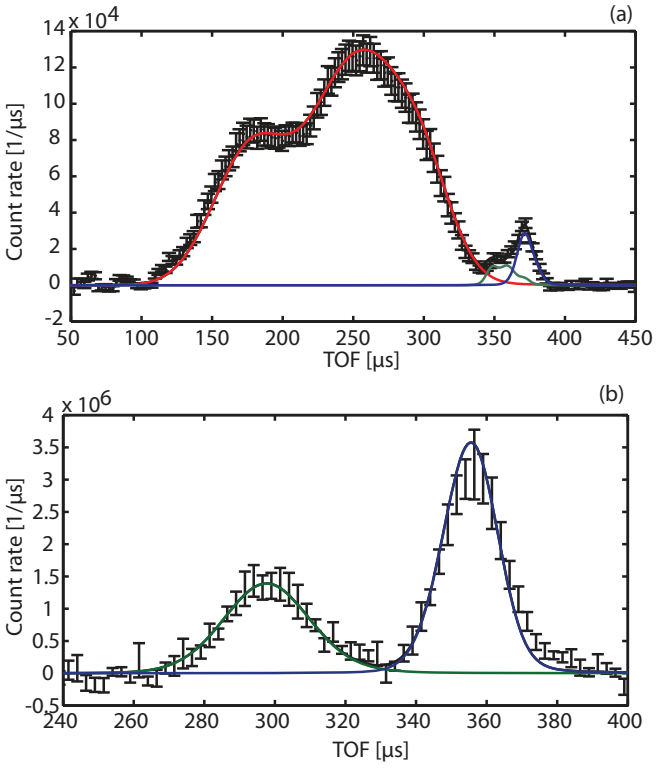

FIG. 12. (Color online) Sum of unit-area-normalized LiH TOF spectra (black symbols) in forward (a) and backscattering (b) compared with the sum of unit-area-normalized individual fits (black line). Individual mass contributions are shown as colored solid lines: red for H, green for Li, and blue for Al.

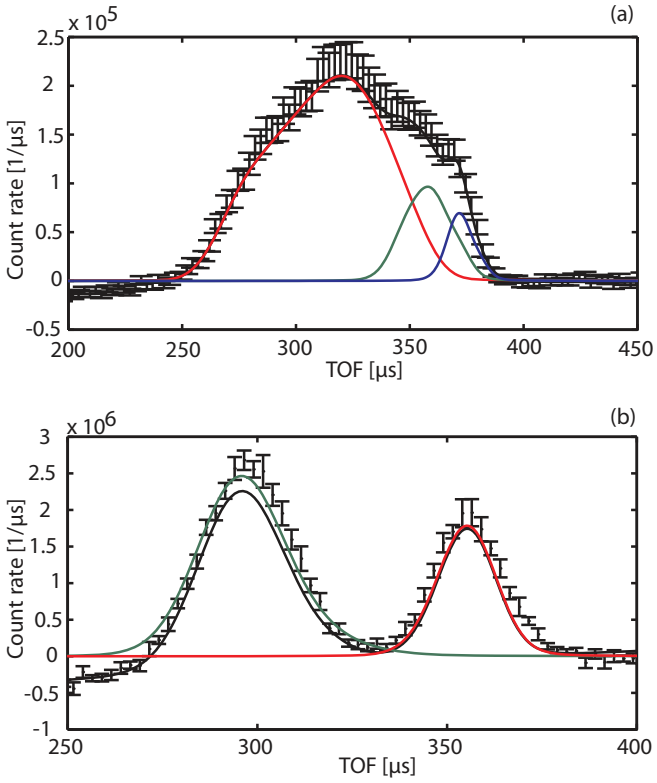

FIG. 13. (Color online) Sum of unit-area-normalized LiD TOF spectra (black symbols) in forward scattering (a) and backscattering (b) compared with the sum of unit-area-normalized individual fits (black line). Individual mass contributions are shown as colored solid lines: red for D, green for Li, and blue for Al.

provided that the resulting NCS line shape is still sensitive to the spectral moments of the underlying NMD. Whereas the viability of this approach is quite clear for backscattering data, further work is required to assess its range of applicability in the forward-scattering direction. To this end, one possibility may involve increasing recoil-peak visibility by focusing specific sets of forward-scattering detectors to yield the best possible peak separation, i.e., in the angular range between 55° and 65°. The other possibility would be the use of summed and normalized foil-in spectra. Here the gain would be twofold, first from a sheer signal-to-noise gain obtained by avoiding the need to perform foil-in/foil-out differencing, and, secondly, from a significant reduction in data-acquisition times.

The results of four separate fitting sessions to describe forward and backscattering data using the models shown in Tables II and III for LiH (LiD) are summarized in Tables IV and V (Tables VI and VII). With these results, it becomes possible to assess the physical validity of these models as well as possible departures from the HBOA and IA in the NCS data. Toward that end, we take the reduced $\langle\chi^2\rangle$ of these fits as our primary figure of merit, along with a consideration of the minimal set of assumptions necessary to describe the experimental data. The values of the reduced $\langle\chi^2\rangle$ listed in Tables IV and V (Tables VI and VII) were obtained from a selected range of spectra recorded in forward and backscattering after removal of faulty detectors and outliers as described in Sec. III B. Average values and associated

TABLE IV. Best-fit parameters for LiH forward-scattering data using the models described in Table II. Asterisks denote fixed parameters.

Model	σ_{H}	k_{H}	$c_{4_{\mathrm{H}}}$	σ_{Li}	k_{Li}	$c_{4_{\mathrm{Li}}}$	σ_{Al}	k_{Al}	$c_{4_{\mathrm{Al}}}$	$\langle\chi^2\rangle$
1	3.5 ± 0.1	0*	0*	6.9 ± 0.3	$\sigma_{\mathrm{Li}}\frac{\sqrt{2}}{12}$	0*	13.39	$\sigma_{\mathrm{Al}}\frac{\sqrt{2}}{12}$	0*	1.19 ± 0.05
2	3.5 ± 0.1	-1.1 ± 0.8	0*	6.9 ± 0.3	$\sigma_{\mathrm{Li}}\frac{\sqrt{2}}{12}$	0*	13.39	$\sigma_{\mathrm{Al}}\frac{\sqrt{2}}{12}$	0*	1.15 ± 0.04
3	3.4 ± 0.1	$\sigma_{\mathrm{H}}\frac{\sqrt{2}}{12}$	-0.12 ± 0.06	7.1 ± 0.5	$\sigma_{\mathrm{Li}}\frac{\sqrt{2}}{12}$	0*	13.39	$\sigma_{\mathrm{Al}}\frac{\sqrt{2}}{12}$	0*	1.21 ± 0.03
4	3.4 ± 0.1	-1.1 ± 0.9	-0.13 ± 0.04	7.0 ± 0.4	$\sigma_{\mathrm{Li}}\frac{\sqrt{2}}{12}$	0*	13.39	$\sigma_{\mathrm{Al}}\frac{\sqrt{2}}{12}$	0*	1.21 ± 0.03
5	3.4 ± 0.1	0*	-0.11 ± 0.06	7.0 ± 0.4	$\sigma_{\mathrm{Li}}\frac{\sqrt{2}}{12}$	0*	13.39	$\sigma_{\mathrm{Al}}\frac{\sqrt{2}}{12}$	0*	1.22 ± 0.03
6	3.5 ± 0.1	$\sigma_{\mathrm{H}}\frac{\sqrt{2}}{12}$	0*	7.0 ± 0.4	$\sigma_{\mathrm{Li}}\frac{\sqrt{2}}{12}$	0*	13.39	$\sigma_{\mathrm{Al}}\frac{\sqrt{2}}{12}$	0*	1.14 ± 0.03

TABLE V. Best-fit parameters for LiH backscattering data using the models described in Table III. Asterisks denote fixed parameters.

Model	σ_{Li}	k_{Li}	$c_{4_{\mathrm{Li}}}$	σ_{Al}	k_{Al}	$c_{4_{\mathrm{Al}}}$	$\langle\chi^2\rangle$
1	9.0 ± 2.1	0*	0*	13.39	$\sigma_{\mathrm{Al}}\frac{\sqrt{2}}{12}$	0*	1.14 ± 0.14
2	9.0 ± 2.1	0.13 ± 3.3	0*	13.39	$\sigma_{\mathrm{Al}}\frac{\sqrt{2}}{12}$	0*	1.15 ± 0.15
3	11.0 ± 1.4	$\sigma_{\mathrm{Li}}\frac{\sqrt{2}}{12}$	0.5 ± 0.8	13.39	$\sigma_{\mathrm{Al}}\frac{\sqrt{2}}{12}$	0*	1.21 ± 0.15
4	9.2 ± 2.1	-0.6 ± 4.3	0.5 ± 0.7	13.39	$\sigma_{\mathrm{Al}}\frac{\sqrt{2}}{12}$	0*	1.22 ± 0.16
5	11.0 ± 1.3	0*	0.5 ± 0.7	13.39	$\sigma_{\mathrm{Al}}\frac{\sqrt{2}}{12}$	0*	1.21 ± 0.15
6	9.0 ± 2.2	$\sigma_{\mathrm{Li}}\frac{\sqrt{2}}{12}$	0*	13.39	$\sigma_{\mathrm{Al}}\frac{\sqrt{2}}{12}$	0*	1.15 ± 0.14

STDs from the mean were calculated from selected groups of reduced $\langle\chi^2\rangle$ values. In forward scattering, average $\langle\chi^2\rangle$ values are in the range 1.11–1.22, with associated STDs of 0.03–0.05 for LiH and 0.15–0.16 for LiD. In backscattering, average $\langle\chi^2\rangle$ values for LiH lie in the range 1.14–1.33, with STDs of 0.14–0.16 for LiH, whereas LiD gives 0.93–0.96 with STDs around 0.17. Within the reported uncertainties, it is important to note that these $\langle\chi^2\rangle$ values are indistinguishable from each other in both LiH and LiD, a strong indicator of the equivalence of all six models within the statistical accuracy of the NCS measurements. Furthermore, we note that NCS widths σ show a consistent degree of insensitivity to the inclusion of higher-order terms in our description of the NMDs. This result suggests that this parameter is particularly robust and largely independent of the underlying physical model used to describe NMDs in both LiH and LiD.

To compare in more detail the results obtained across all four fitting sessions, we make recourse to Ockham's razor. In this spirit, the best description of the underlying NMDs is given by the model involving the smallest number of independent fitting parameters and with $\langle\chi^2\rangle$ sufficiently close to unity. This exercise provides an exhaustive and hitherto unattempted analysis of the sensitivity of the measured TOF data to the width of the NMDs, as well as to the inclusion of higher-order corrections. On the basis of these considerations, model 6 constitutes the simplest one of the set, as it describes a Gaussian momentum distribution ($c_4 = 0$) and FSEs compliant with the 3D-HO model ($k_M = \sigma_M \frac{\sqrt{2}}{12}$) for all nuclei. Moreover, model 6 gives $\sigma_{\mathrm{H}} = 3.5 \pm 0.1$ Å^{-1} and $\sigma_{\mathrm{Li}} = 7.0 \pm 0.4$ Å^{-1} in forward scattering, in excellent agreement with previous *ab initio* calculations ($\sigma_{\mathrm{H}} = 3.57$ Å^{-1} and $\sigma_{\mathrm{Li}} = 7.14$ Å^{-1}).[2] For LiD, the same model gives $\sigma_{\mathrm{D}} = 4.4 \pm 0.1$ Å^{-1} and $\sigma_{\mathrm{Li}} = 7.2 \pm 0.9$ Å^{-1} in forward scattering. These values are within one STD from *ab initio* predictions, namely $\sigma_{\mathrm{D}} = 4.43$ Å^{-1} and $\sigma_{\mathrm{Li}} = 7.15$ Å^{-1}. Although considerably less accurate, the widths of the Li momentum distributions in backscattering are also consistent with the above results, with values for σ_{Li} of 9.0 ± 2.2 and 7.0 ± 0.8 Å^{-1} for LiH and LiD, respectively.

Our results and accompanying analysis indicate that both the HBOA and the Sears model to account for FSEs are sufficient to describe our experimental data. Any deviations from the IA beyond Sears predictions are sensibly below present instrumental capabilities. Moreover, NMDs of H, D, and Li in LiH and LiD are adequately described via the use of Gaussian NCS profiles $J(y)$, thus also confirming the validity of the GA to describe our experimental NCS data.

V. DISCUSSION

In previously reported first-principles calculations,[2] the NMD second moment σ as well as the Laplacian of the effective Born-Oppenheimer potential Δ were calculated quantum mechanically based on a PW-DFT approach for optimized cubic LiH and LiD crystal cells. The GGA-PBE functional[52] was used in these calculations, and NCS observables were calculated within a strictly harmonic description of all nuclear motions. These *ab initio* results for cubic LiH agreed very well with proton kinetic energies obtained from past NCS and INS experiments at 20 and 300 K.[3,5] The *ab initio* value of $\sigma_{\mathrm{H}} = 3.57$ Å^{-1} at $T = 300$ K was only ∼2% larger than 3.49 ± 0.05 Å^{-1}, corresponding to the isotropic average obtained from previous NCS measurements at the same temperature.[4,5] Moreover, *ab initio* predictions at $T = 20$ K ($\sigma_{\mathrm{H}} = 3.49$ Å^{-1}) fell between previously reported experimental values, namely 3.44 Å^{-1} (NCS measurements)[4] and 3.59 Å^{-1} (INS measurements).[5] Also, *ab initio* values for the isotropically averaged Δ in LiH agreed well with those obtained in NCS and INS experiments assuming an isotropic

TABLE VI. Best-fit parameters for LiD forward-scattering data using the models described in Table II. Asterisks denote fixed parameters.

Model	σ_{D}	k_{D}	$c_{4_{\mathrm{D}}}$	σ_{Li}	k_{Li}	$c_{4_{\mathrm{Li}}}$	σ_{Al}	k_{Al}	$c_{4_{\mathrm{Al}}}$	$\langle\chi^2\rangle$
1	4.4 ± 0.1	0*	0*	7.0 ± 1.0	$\sigma_{\mathrm{Li}}\frac{\sqrt{2}}{12}$	0*	13.39	$\sigma_{\mathrm{Al}}\frac{\sqrt{2}}{12}$	0*	1.17 ± 0.14
2	4.4 ± 0.1	0.1 ± 0.4	0*	7.0 ± 1.0	$\sigma_{\mathrm{Li}}\frac{\sqrt{2}}{12}$	0*	13.39	$\sigma_{\mathrm{Al}}\frac{\sqrt{2}}{12}$	0*	1.16 ± 0.14
3	4.4 ± 0.4	$\sigma_{\mathrm{D}}\frac{\sqrt{2}}{12}$	-0.02 ± 0.2	7.2 ± 1.0	$\sigma_{\mathrm{Li}}\frac{\sqrt{2}}{12}$	0*	13.39	$\sigma_{\mathrm{Al}}\frac{\sqrt{2}}{12}$	0*	1.27 ± 0.15
4	4.8 ± 0.9	-0.1 ± 0.4	0.2 ± 0.4	7.0 ± 1.1	$\sigma_{\mathrm{Li}}\frac{\sqrt{2}}{12}$	0*	13.39	$\sigma_{\mathrm{Al}}\frac{\sqrt{2}}{12}$	0*	1.33 ± 0.14
5	4.8 ± 0.8	0*	0.2 ± 0.4	7.1 ± 1.1	$\sigma_{\mathrm{Li}}\frac{\sqrt{2}}{12}$	0*	13.39	$\sigma_{\mathrm{Al}}\frac{\sqrt{2}}{12}$	0*	1.25 ± 0.15
6	4.4 ± 0.1	$\sigma_{\mathrm{D}}\frac{\sqrt{2}}{12}$	0*	7.2 ± 0.9	$\sigma_{\mathrm{Li}}\frac{\sqrt{2}}{12}$	0*	13.39	$\sigma_{\mathrm{Al}}\frac{\sqrt{2}}{12}$	0*	1.18 ± 0.15

TABLE VII. Best-fit parameters for LiD backscattering data using the models described in Table III. Asterisks denote fixed parameters.

Model	σ_{Li}	k_{Li}	$c_{4_{\mathrm{Li}}}$	σ_{Al}	k_{Al}	$c_{4_{\mathrm{Al}}}$	$\langle\chi^2\rangle$
1	7.0 ± 0.8	0*	0*	13.39	$\sigma_{\mathrm{Al}}\frac{\sqrt{2}}{12}$	0*	0.94 ± 0.17
2	7.1 ± 0.9	0.6 ± 1.8	0*	13.39	$\sigma_{\mathrm{Al}}\frac{\sqrt{2}}{12}$	0*	0.94 ± 0.17
3	7.2 ± 1.5	$\sigma_{\mathrm{Li}}\frac{\sqrt{2}}{12}$	0.0 ± 0.6	13.39	$\sigma_{\mathrm{Al}}\frac{\sqrt{2}}{12}$	0*	0.99 ± 0.14
4	7.2 ± 1.5	0.4 ± 2.2	0.4 ± 0.7	13.39	$\sigma_{\mathrm{Al}}\frac{\sqrt{2}}{12}$	0*	0.99 ± 0.14
5	7.5 ± 1.5	0*	0.1 ± 0.6	13.39	$\sigma_{\mathrm{Al}}\frac{\sqrt{2}}{12}$	0*	0.99 ± 0.14
6	7.0 ± 0.8	$\sigma_{\mathrm{Li}}\frac{\sqrt{2}}{12}$	0*	13.39	$\sigma_{\mathrm{Al}}\frac{\sqrt{2}}{12}$	0*	0.93 ± 0.17

3D-HO model. A theoretical value of $\Delta = 7622$ meV Å^{-2} for H in LiH was also intermediate between experimental values of 6968 and 8265,[4,5] and only 3% above NCS experiments at 300 K.[4] On the whole, no evidence was found for the postulated broadening of the H NMD in solid LiH originating from a breakdown of the Born-Oppenheimer approximation.[26,53,54] In and of itself, comparison of previous experimental data[3,5] with these theoretical predictions[2] served to demonstrate the possibility of using the NCS technique for the reliable measurement of NMDs beyond H and D.

The NCS experiments mentioned above were performed using a previous detector configuration of the VESUVIO spectrometer.[4,5] Since then, the overall resolution of the NCS method has been greatly improved on VESUVIO.[32] These recent developments should allow, in principle, access to finer changes in line shape and/or shifts in recoil features than previously accessible, as well as the possibility of testing more subtle effects associated with nonadiabatic effects in quantum nuclear dynamics.[26,53,54] These improvements in accuracy and resolution in backscattering geometry have already enabled MANSE studies for moderate-mass systems such as ^{7}LiF,[18] yet parallel efforts exploiting neutron detection in both forward and backscattering directions have not been attempted prior to the present work. The results presented here for H, D, and Li demonstrate the feasibility of the approach.

Guided by Ockham's razor, we have also carried out a detailed analysis so as to select the most appropriate model for the underlying NMDs. From this analysis, we conclude that the GA provides a satisfactory description of NMDs and that possible higher-order effects are sufficiently small such that their overall influence on the estimation of second moments σ for H, D, and Li is practically negligible in both LiH and LiD. Moreover, our analysis of the experimental data gives values of σ and k which are fully consistent with *ab initio* HBOA predictions,[2] as well as with the absence of detectable nonadiabatic effects in the NCS response of these fcc solids. Conversely, the fact that the above *ab initio* predictions of the VDOSs and phonon-dispersion relations lead to isotropic σ and k values further reinforces the notion that the underlying NMDs for H, D, and Li in LiH and LiD are well accounted for within the GA.

Notwithstanding the above, the apparent absence of departures from the Born-Oppenheimer approximation in our NCS experiments does not necessarily imply that other (and equally interesting) effects could not be verified using the current incarnation of the NCS spectrometer VESUVIO. One of these, as recently postulated by Karlsson,[11] relates to the elastic slowing-down of recoiling H and D during the scattering process, as described by the Watson scattering time.[7] For the case of diatoms, Karlsson presents an alternative treatment of FSEs leading to quantitative results that differ from those of the standard (and widely used) treatment of Sears.[13,14] In essence, there are two main differences between these two approaches, namely (i) the skewness of the NMD scales differently from Sears predictions, as it becomes proportional to the expectation value of Δ, as well as inversely proportional to the magnitude of neutron-momentum transfer; and (ii) the resulting NMDs show quantitative differences compared to the Sears result in the high-energy tail of the NCS profiles. In simple terms, the arguments put forth by Karlsson are predicated on the assumption that at very short (albeit finite) scattering times, different sets of vibrational levels are accessed by the recoiling nucleus during a given NCS event. Thus, different values of the neutron-momentum transfer translate into a different extent of averaging over vibrational levels, naturally leading to an overall non-Gaussian NMD. In the IA limit, we recall that the standard treatment by Sears would predict a Gaussian line shape. Such a nonuniform averaging is specially pronounced for diatomic molecules such as H_2 and D_2, as their vibrational levels are far apart, thereby precluding vibrational excitation at low scattering angles. LiH (LiD) vibrational-stretch motions are approximately four times slower than in H_2 (D_2), and in this regime our results conform with the expectations of the Sears treatment of the NCS process. Specifically, the magnitude of FSE contributions remains constant with increasing scattering angle for all three nuclei under consideration. In the spirit of the approach by Karlsson, and considering that the LiH molecule can be treated as a fixed target, excitation to the lowest vibrational state takes place at a momentum transfer of $\sim$9 Å^{-1}, a value sensibly smaller than in the case of H_2 ($\sim$16 Å^{-1}). These differences in momentum transfer imply that the elastic slowing-down of the recoiling H and D nuclei in LiH and LiD will be less pronounced than in the case of the lighter H_2 or D_2, thus leading to NMDs much closer to the IA limit at smaller forward-scattering angles.

On the whole, our experimental results and accompanying data analysis yield no apparent departures from Sears scaling due to the elastic-slowing-down mechanism postulated by Karlsson, effects which would manifest themselves as extra scattering intensity in the high-energy tails of the NCS profile compared to the (purely symmetrical) IA result. This conclusion is further corroborated by the absence of FSEs or higher-order terms in the Gram-Charlier expansion for the

NMDs of H, D, and Li beyond those expected within the GA and *ab initio* HBOA predictions.

VI. OUTLOOK

We have reported NCS measurements for solid LiH and LiD. With the present experimental setup, we demonstrate the ability to perform detailed and simultaneous MANSE studies on H, D, and Li in forward and backscattering geometries. Moreover, our strategy allowed for an assessment of deviations from *ab initio* HBOA predictions and the IA. The measured widths of H, D, and Li NMDs in solid LiH and LiD are in very good agreement with previously reported *ab initio* calculations within the HBOA. This result further demonstrates the validity of these approximations for first-principles predictions of NCS observables. LiH and LiD have also been tested for the existence of elastic-slowing-down effects as recently postulated by Karlsson. On the whole, our analysis yields no departures from Sears scaling within experimental uncertainties, a conclusion which is reinforced by the observed magnitudes of FSEs as well as their compliance with the HBOA. Our extensive experimental results also confirm an upper bound of a few % for the effects of nonadiabatic dynamics on the second moment σ and Laplacian Δ of the underlying NMDs, in agreement with previous theoretical and experimental studies of these systems.

Heavier nuclei characterized by $m > 4$ amu remain a challenge to NCS techniques, and much work still remains to be done in order to provide access to the fine details of these NMDs relative to what is possible at present with either H or D. In the case of Li, the present work has shown that such a task is possible in both forward and backscattering geometries. The latter case could greatly benefit from further improvements in DD techniques for final-energy selection. In addition to a sheer increase in incident neutron flux, implementation of detector-focusing techniques also offers the exciting prospects of order-of-magnitude gains in effective count rates, thereby paving the way for routine MANSE investigations of complex materials as well as detailed parametric studies as a function of external stimuli.

ACKNOWLEDGMENTS

The authors gratefully acknowledge the UK Science & Technology Facilities Council for financial support under Contract No. PR1200068 and access to beamtime at the ISIS Facility.

*matthew.krzystyniak@stfc.ac.uk

†also at Department of Physics and Astronomy, University College London, Gower Street, London WC1E 6BT, United Kingdom; felix.fernandez-alonso@stfc.ac.uk

[1] M. Krzystyniak, J. Chem. Phys. **133**, 144505 (2010).
[2] M. Krzystyniak and F. Fernandez-Alonso, Phys. Rev. B **83**, 134305 (2011).
[3] J. Boronat, C. Cazorla, D. Colognesi, and M. Zoppi, Phys. Rev. B **69**, 174302 (2004).
[4] T. Abdul-Redah, P. A. Georgiev, M. Krzystyniak, D. K. Ross, and C. A. Chatzidimitriou-Dreismann, Physica B **385-386**, 57 (2006).
[5] D. Colognesi, A. J. Ramirez-Cuesta, M. Zoppi, R. Senesi, and T. Abdul-Redah, Physica B **350**, E983 (2004).
[6] M. Krzystyniak, M. A. Adams, A. Lovell, N. T. Skipper, S. M. Bennington, J. Mayers, and F. Fernandez-Alonso, Faraday Discuss. **151**, 171 (2011).
[7] G. I. Watson, J. Phys.: Condens. Matter **8**, 5955 (1996).
[8] C. Andreani, D. Colognesi, J. Mayers, G. F. Reiter, and R. Senesi, Adv. Phys. **55**, 377 (2005).
[9] A. Pietropaolo and R. Senesi, Phys. Rep. **508**, 45 (2011).
[10] L. A. Rodríguez Palomino, J. J. Blostein, and J. Dawidowski, J. Instrum. **8**, P08016 (2013).
[11] E. B. Karlsson, Nucl. Instrum. Methods A **694**, 286 (2012).
[12] C. Andreani, D. Colognesi, and E. Pace, Phys. Rev. B **60**, 10008 (1999).
[13] V. F. Sears, Phys. Rev. B **30**, 44 (1984).
[14] V. F. Sears, Phys. Rev. A **7**, 340 (1973).
[15] A. S. Rinat, Phys. Rev. B **36**, 5171 (1987).
[16] A. Gersch, L. J. Rodriguez, and P. N. Smith, Phys. Rev. A **5**, 1547 (1972).
[17] V. G. Plekhanov, Mater. Sci. Eng. R **35**, 139 (2001).
[18] A. G. Seel, M. Ceriotti, and P. P. Edwards, J. Phys.: Condens. Matter **24**, 365401 (2012).
[19] J. M. F. Gunn, C. Andreani, and J. Mayers, J. Phys. C **19**, L835 (1986).
[20] J. Mayers, C. Andreani, and G. Baciocco, Phys. Rev. B **39**, 2022 (1989).
[21] J. Mayers, Phys. Rev. B **41**, 41 (1990).
[22] J. Mayers, Phys. Rev. Lett. **71**, 1553 (1993).
[23] J. Mayers and T. Abdul-Redah, J. Phys.: Condens. Matter **16**, 4811 (2004).
[24] G. B. West, Phys. Rep. C **18**, 263 (1975).
[25] A. Fielding, D. N. Timms, and J. Mayers, Europhys. Lett. **44**, 255 (1998).
[26] G. F. Reiter and P. M. Platzman, Phys. Rev. B **71**, 054107 (2005).
[27] R. Senesi, D. Colognesi, A. Pietropaolo, and T. Abdul-Redah, Phys. Rev. B **72**, 054119 (2005).
[28] R. Senesi, D. Flammini, A. I. Kolesnikov, E. D. Murray, G. Galli, and C. Andreani, J. Chem. Phys. **139**, 074504 (2013).
[29] D. Flammini, A. Pietropaolo, R. Senesi, C. Andreani, F. McBride, A. Hodgson, M. Adams, L. Lin, and R. Car, J. Chem. Phys. **136**, 024504 (2012).
[30] C. Andreani, D. Colognesi, E. Degiorgi, and M. A. Ricci, J. Chem. Phys. **115**, 11243 (2001).
[31] R. Senesi, C. Andreani, Z. Bowden, D. Colognesi, E. Degiorgi, A. L. Fielding, J. Mayers, M. Nardone, J. Norris, M. Praitano *et al.*, Physica B **276**, 200 (2000).
[32] S. Imberti, C. Andreani, V. Garbuio, G. Gorini, A. Pietropaolo, R. Senesi, and M. Tardocchi, Nucl. Instrum. Methods A **552**, 463 (2005).

[33]E. P. Cippo, G. Gorini, M. Tardocchi, C. Andreani, A. Pietropaolo, R. Senesi, N. J. Rhodes, and E. M. Schoonveld, Meas. Sci. Technol. **19**, 047001 (2008).
[34]M. Tardocchi, G. Gorini, A. Pietropaolo, C. Andreani, R. Senesi, N. Rhodes, and E. Schooneveld, Rev. Sci. Instrum. **75**, 4880 (2004).
[35]C. Andreani, A. Pietropaolo, R. Senesi, G. Gorini, E. Perelli-Cippo, M. Tardocchi, N. Rhodes, and E. Schooneveld, Appl. Phys. Lett. **85**, 5454 (2004).
[36]E. M. Schooneveld, J. Mayers, N. J. Rhodes, A. Pietropaolo, C. Andreani, R. Senesi, G. Gorini, E. Perelli-Cippo, and M. Tardocchi, Rev. Sci. Instrum. **77**, 095103 (2006).
[37]A. Seeger, A. D. Taylor, and R. M. Brugger, Nucl. Instrum. Methods A **240**, 98 (1985).
[38]C. Andreani, D. Colognesi, E. Degiorgi, A. Filabozzi, M. Nardone, E. Pace, A. Pietropaolo, and R. Senesi, Nucl. Instrum. Methods Phys. Res. A **497**, 535 (2003).
[39]J. J. Blostein, J. Dawidowski, and J. R. Granada, Physica B **334**, 257 (2003).
[40]J. J. Blostein, J. Dawidowski, S. A. Ibanez, and J. R. Granada, Phys. Rev. Lett. **90**, 105302 (2003).
[41]T. Abdul-Redah, M. Krzystyniak, and C. A. Chatzidimitriou-Dreismann, Phys. Rev. B **72**, 052202 (2005).
[42]J. Mayers and M. A. Adams, Nucl. Instrum. Methods A **625**, 47 (2011).
[43]A. Pietropaolo, C. Andreani, A. Filabozzi, E. Pace, and R. Senesi, Nucl. Instrum. Methods A **570**, 498 (2007).
[44]S. W. Lovesey, *Theory of Neutron Scattering from Condensed Matter* (Clarendon, Oxford, 1984).
[45]J. Mayers, A. Fielding, and R. Senesi, Nucl. Instrum. Methods A **481**, 454 (2002).
[46]J. Mayers, Meas. Sci. Technol. **22**, 015903 (2011).
[47]M. Krzystyniak and T. Abdul-Redah, Phys. Rev. B **82**, 064301 (2010).
[48]C. Y. Ho, R. W. Powell, and P. E. Liley, J. Phys. Chem. Ref. Data **1**, 279 (1972).
[49]H. R. Glyde, Phys. Rev. B **50**, 6726 (1994).
[50]H. W. Press, S. A. Teukolsky, W. T. Vetterling, and B. P. Flannery, *Numerical Recipes in Fortran 77: The Art of Scientific Computing*, 2nd ed. (Cambridge University Press, New York, 1992).
[51]J. Mayers and G. Reiter, Meas. Sci. Technol. **23**, 045902 (2012).
[52]J. P. Perdew, K. Burke, and M. Ernzerhof, Phys. Rev. Lett. **77**, 3865 (1996).
[53]N. I. Gidopoulos, Phys. Rev. B **71**, 054106 (2005).
[54]I. E. Mazets, C. A. C.-Dreismann, and G. Kurizki, in *Decoherence, Entanglement and Information Protection in Complex Quantum Systems*, edited by V. M. Akulin, A. Sarfati, G. Kurizki, and S. Pellegrin, Vol. 189 (Springer, Dordrecht, 2005), p. 549.